Characterisation and Optimisation of a Real-Time Diesel engine model

PG Dowell, S Akehurst, RD Burke

Powertrain and Vehicle Research Centre, Department of Mechanical Engineering, University of Bath, Bath, BA2 7AY

Abstract

Accurate real time engine models are an essential step to allow the development of control algorithms in parallel to the development of engine hardware using hardware in the loop application. A physics-based model of the engine high-pressure air path and combustion chamber is presented. The model has been parameterised using data from a small set or carefully selected operating conditions for a 2.0L Diesel engine. The model has subsequently been validated over the complete engine operating map with and without EGR. A high level of fit was achieved with R^2 value above 0.94 for mean effective pressure and above 0.99 for air flow rate.

Model run-time was then reduced for real-time application by using forward differencing; single precision floating point numbers; and by only calculating in-cylinder prediction for a single cylinder. A further 25% improvement in run time was achieved by improving sub-models, including the strategic use of 1D/2D look-up tables with optimised resolution. The model exceeds the performance of similar models in the literature achieving 0.5°CA resolution at 4000rev/min. This simulation step size

still yields good accuracy compared to 0.1°CA resolution and has been validated against experimental results from an NEDC drive cycle. The real-time model will allow the development of control strategies before the engine hardware is available, meaning more time can be spent ensuring the engine can meet performance and emissions requirements over it full operating range.

Key Words: Diesel Engine, Hardware in the Loop, Real Time Model, Filling and Emptying, Mixing Controlled Combustion Model

1 Introduction

With increasingly aggressive duty cycles being introduced such as the World Harmonized Test Cycle (WLTC) and Real Driving Emissions (RDE) engine manufacturers will need to dedicate considerably more effort to meet emissions requirements from diesel engines [1]. For the engine, this includes the optimisation of control set-points for features such as exhaust gas recirculation (EGR); multi-stage, variable geometry turbochargers (VGT); high-pressure common-rail direct injection fuel injectors; and variable valve openings. This presents a huge engineering challenge for the development of control and fault detection strategies [2] that would be too time consuming using conventional hardware based approaches.

Hardware in the Loop (HiL) is a model based approach where the controller can be developed concurrently to engine hardware by using a mathematical model emulating the engine behaviour. The key enabler of this approach is the availability of high accuracy models with low computational run-times that can be parameterised using minimal experimental data. To be able to run in a HiL

configuration, the model should also be able to predict in-cycle quantities to simulate real sensor feedback, such as pressure, both in the air path and the combustion chamber

This paper aims to create and a real-time capable model of the engine cylinder and combustion process that can predict crank-angle-resolved in-cylinder pressure. To provide crank angle resolved boundary conditions to the cylinder, a simplified model of the high-pressure air-path is necessary and will also be presented (exhaust and intake manifolds, EGR cooler and EGR valve). The turbocharger and low pressure air path is outside the scope of this work.

The key model inputs will be:

- Turbocharger Compressor outlet temperature and pressure
- Engine Speed
- Exhaust manifold pressure
- Cylinder wall temperature
- Injector driver signal and rail pressure
- EGR valve position

The key model outputs will be:

- In-cylinder Pressure
- Rate of Heat Release
- Exhaust temperature
- Mass Flow rate

The key contributions of this work are the novel experimental technique to parameterise the real-time model and the refinement of the model structure to improve run-time. After reviewing the background to this work in section 2, the model and its experimental characterisation will be presented in sections 3 and 4. Section 5 will show the experimental validation and finally in section 6 the run-time optimisation and real-time model validation will be presented.

2 Background

2.1 Engine modelling

Engine models can be broadly separated into three categories in order of increasing physical fidelity and run-time: mean-value models (MVEM); filling and emptying models; and wave action (method of characteristics) models [3]. Increasing model complexity brings insight into the internal processes of the system but at the expense of increased running time [4]. The difference in model types stems from their temporal and spatial resolution.

- MVEMs operate on a cycle by cycle basis to provide average performance metrics for the engine. They can easily be made to run many times faster than real-time and are often used in model-based optimal controllers [3-7].
- Filling and emptying models operate on a similar special resolution to MVEMs, but simulate the behaviour within the cycle to provide a crank angle resolved estimate of performance metrics (pressures, torques, temperatures…)

- Gas Dynamic models are constructed with similar time resolution to filling and emptying models, but incorporate a larger special resolution to capture the effects of pressure waves and gas dynamics.

2.1.1 Mean Value Engine models

Mean value engine models (MVEMs) neglect the engine breathing dynamics and consider the performance as an average over the combustion cycle. Early MVEMs were essentially build as look-up tables, indexing operating parameters such as torque, Indicated mean effective pressure (IMEP), volumetric efficiency and emissions as functions of fuelling, operating speed, and other control parameters [2]. These models require significant amounts of data to be parameterised [3, 8-10] and can only provide a reliable model of engine performance within the ranges that they have been trained [11, 12]. The amount of data increases significantly if emissions are to be modelled [13]. The accuracy of the model is largely dependent on the accuracy of the measured data [14], and to adapt the model for another engine, new data from the new engine is required [3, 14, 15].

Thermodynamic based MVEMs [16] are constructed based on ideal thermodynamic processes which incorporate some description of the underlying physics. These types of models are typically built around ideal thermodynamic cycles calculate gas states at the end of each process within the cycle. These types of models are slower than the data-driven models, but still sufficiently fast to run many times real-time and therefore suitable for controller development. The inclusion of the thermodynamic relationships allows this type of MVEM to estimate some in-cycle quantities such as peak cylinder pressure and temperature. These are a promising modelling approach that could

bridge the gap between data driven MVEMs and Filling and emptying models because the key in-cycle quantities can be linked to emissions models reducing the required amount of parameterisation data.

MVEM are suitable for powertrain modelling because the driveline dampens the combustion pulses [17]. Due to their compact nature, these models often can run many times faster than real-time [18], and offer reasonable accuracy over drive cycle timescales making them an enabler of model based optimal control strategies. However, the lack of details during the combustion event can be limiting as the shape of the heat release rate and in-cylinder pressure are unknown. This is important during combustion for estimating the formation of emissions [19] but also during intake and exhaust strokes to correctly estimate engine breathing which in a MVEM is inferred from an empirical volumetric efficiency [20]. This effect can be amplified during transients, as with a dynamic model of the engine air path as turbochargers and EGR paths create an inherent feedback loop within the model. Hendricks et al. claim accuracy of ±2% over the whole operating range, falling to ±10% during transient performance [14]. Hunt et al. estimate the accuracy of these models to be a more conservative ±10-15% [21].

2.1.2 Filling and emptying models

Filling and emptying models operate on a much finer timescale than that of mean-value models, typically on a crank-angle resolved basis [15, 22]. In this way, these models can predict the evolution of in-cylinder pressure and mass flow through the valves throughout the cycle. The system is broken down into a small number of discrete control volumes (such as the cylinders and intake/exhaust

manifolds) which are ‘emptying’ and ‘filling’ in turn as gases move through the engine [22]. Energy conservation equations and the equations of flow through a restricted orifice are used to define the state of the gas in each control volume. Each chamber is treated as an open system of fixed volume which contains gas at a uniform state. Typically, if the time it takes a pressure wave to travel twice the length of the manifold is less than 15-20°CA, then the error introduced by this assumption will be negligible [22]. This approach lends itself to achieving faster running times than more gas dynamic models, whilst retaining adequate complexity to make accurate predictions on a crank angle resolved basis [23]. This makes the filling and emptying model suitable for HiL development of engine controllers where maintaining the engine dynamics during the cycle is important if in-cylinder pressure feedback is to be used. The challenge for such models is to reduce the complexity to a level that can run real-time without significantly compromising accuracy.

2.1.3 Wave action models

Wave actions models are built on a similar principle to filling and emptying models, although the pipework of the engine is discretised into a greater number of smaller control volumes. This allows to the calculation of pressure waves throughout the system which is important for tuning of manifold lengths. The greater number of control volumes significantly increases the calculation time of the model to multiple times real time. The greater accuracy of engine breathing events means these models are ideally suited for engine design but cannot be used in real-time applications using HiL configurations.

2.2 Hardware-in-the-loop and real-time modelling

A conventional HiL engine model consists of a mathematical model of the engine running on a real-time DSP connected to an input/output (I/O) board that provides communication between physical actuators (such as injectors, common rail, fuel pump, and EGR / VGT actuators) and the ECU [2]. For the developed model to be suitable for HiL applications, it must first meet the following requirements:

- The simulation must use a fixed timestep to run on embedded hardware [12, 24]
- The simulation must be numerically stable and accurate, to not cause any faults when interacting with connected hardware [24, 25]
- The simulation must run in real-time (RT); that is step size must be greater than computation time at every time step without overruns to avoid hardware faults [2, 12, 24, 26, 27]

Many existing examples of real-time engine models exist, however most are mean value engine models (MVEM) and neglect in-cylinder dynamics [2, 12]. Since these models typically work on a cyclic basis, they operate on a relatively large time step of approximately 5ms on a 1GHz Pentium PC with 512MB, although the authors acknowledge this is a crude assessment of model performance [27].

Table 1 shows the performance of three recent real-time engine models from the literature with in-cylinder pressure prediction demonstrating that it is possible to predict in-cylinder pressure in real time with current hardware.

Table 1 – Real time performance of combustion models with in-cylinder prediction from recent studies

Reference	Model Type	Step Size (µs)	CA resolution at 4000rpm	Platform
[2] [12]	Single zone Mixing controlled model combustion model with mean value filling and emptying air path model	100	2.40	dSpace DS1006 at 2.6GHz
[11]	Wiebe shape combustion model with discretised air path with 0D ducts and lumped capacitances	27.8	0.66	Intel Xeon at3.66GHz
[21]	Not-disclosed combustion model with 0D ducts and lumped capacitances	33.3	0.80	dSpace Power PC 750 at 480MHz

3 Model configuration

The air path is composed of a series of sub-models that capture the flow of gas through each component using the filling and emptying methodology. An overview of the filling and emptying components is shown in Figure 1. Only the high-pressure part of the air-path is considered (neglecting the turbocharger, air filter and exhaust after-treatment). The high-pressure gas path is split into four control volumes: The cylinder, EGR path and intake and exhaust manifolds. The control volumes are linked using models of the intake, exhaust and EGR valves. In each control volume, the gas is considered to be composed of up to three species: fresh air, fuel and burnt fuel and air. A gas properties model was used to determine the bulk fluid properties in each case. The following sections detail each of these sub models.

3.1 Intake and exhaust manifolds

Both the intake and exhaust manifolds are modelled as thermodynamic control volumes using mass and energy balances to determine the rate of change of mass and energy across the volume [2, 4, 12].

The inlet manifold has two mass flow and temperature inputs (fresh air and EGR cooler) and a single exit port (into the engine cylinder). The intake manifold was assumed to be adiabatic as the gas temperature are relatively low. In this work the turbocharger was not modelled and the pressure in the intake manifold and temperature of the fresh air was imposed. The temperature in the manifold was calculated based on the assumption of perfect mixing of EGR and fresh air. The flow of fresh air was assumed to be sufficient to maintain the imposed pressure. In a real engine, this pressure would be a result of flow from the turbocharger, however the approach is a reasonable approximation of a well-matched turbocharger operating with a tuned boost controller. The flow into the engine depends on the dynamics of the intake valve and the in-cylinder conditions described by the in-cylinder sub-model.

In the exhaust manifold, the pressure was again imposed based on measured values. In practice this would result from the flow restriction created by the turbocharger turbine. Gases flow from the cylinder to the exhaust manifold and exit through the EGR cooler and exhaust line. Heat transfer must be considered in the exhaust manifold and exhaust ports to give an accurate estimate of inlet temperature at the turbine [4, 22]. It was assumed that the dominant form of heat transfer was

forced convection. Assuming turbulent gas flow and homogeneous temperatures, an expression for the heat transfer coefficient is given by Zweiri et al. [28]:

$$h_{conv} = 0.023 \frac{k_{gas}}{D} Re^{0.8} Pr^{0.3} \quad \mathbf{1}$$

A physics based, lumped capacitance model of exhaust port and manifold temperature is beyond the scope of this paper which focusses on the combustion chamber. Therefore, an empirical approach was used to determine a bulk port and manifold wall temperature. Figure 2 shows that over the range of the engine map there was a strong trend in exhaust temperature with increasing fuel demand. Therefore, it was decided that the most appropriate model for exhaust manifold wall temperature would be a quadratic fit to fuel demand, since wall temperature will be proportional to gas temperature. This empirical model was determined by firstly fitting a quadratic expression to measured exhaust gas temperature at the inlet to the turbocharger. This fitted gas temperature was then used to determine the bulk wall temperature. This results in a quadratic expression for bulk wall temperature as a function for total fuelling as shown in Equation 2.

$$T_{exh,wall} = a_1 \dot{m}_f^2 + a_2 \dot{m}_f + a_3 \quad \mathbf{2}$$

3.2 Valve models

Inlet, exhaust and EGR valves were modelled assuming adiabatic, isentropic flow. Mass flow was calculated under a known pressure ratio given a reference throat area A_{valve} and an empirically derived discharge coefficient C_d [12, 29]:

$$\dot{m}_{valve} = A_{valve} C_d \frac{p_i}{\sqrt{RT_i}} \Psi\left(\frac{p_j}{p_i}, \gamma\right) \quad \mathbf{3}$$

The flow function (Ψ) is governed by the pressure ratio between the downstream pressure (subscript *j*) and the upstream stagnation pressure (subscript *i*) and related to the ratio of specific heats (γ) [12], (see equation 32 in Appendix A1). Since the instantaneous flow velocities are relatively small, the static pressure upstream of the valves can be taken to be approximately equal to the stagnation pressure [30]. The reference valve area for inlet and exhaust valves depends on the valve lift and geometry as described in equation 33 in Appendix A [29]. The discharge coefficients for the inlet and exhaust valves were found as a function of valve lift from measurement on a flow bench. Typical results of these calculations are illustrated in Figure 20.

The EGR valve characteristics were determined experimentally based on measured EGR flow rates. This data could also be provided by flow bench characterisation of the valve. An empirical equation describing valve flow area as a function of EGR valve lift and engine speed was used (Equation 6). As shown in Figure 3, the main effect is the valve opening, however there is non-negligible trend with engine speed. The inclusion of engine speed was necessary to capture a more accurate trend in effective valve area for this model. The effect of flow pulsations could explain this correlation. The

EGR flow rate is measured on a cycle average basis using inlet and exhaust CO_2 concentrations and by computing a CO_2 balance on the mixing junction of fresh air and EGR (equation 4).

$$\dot{m}_{air}u_{CO2}c_{CO2,amb} + \dot{m}_{EGR}u_{CO2}c_{CO2,ex} = (\dot{m}_{air} + \dot{m}_{EGR})u_{CO2}c_{CO2,in} \quad \mathbf{4}$$

Where u_{CO2} is taken from BS ISO8178-1:2006 [31]

By assuming the ambient CO2 concentration is negligible, equation 4 can be rearranged to give an expression for EGR mass flow rate

$$\dot{m}_{EGR} = \dot{m}_{air}\frac{c_{CO2,in}}{c_{CO2,ex}}\frac{1}{1-\frac{c_{CO2,in}}{c_{CO2,ex}}} = \dot{m}_{air}\left(1+\frac{1}{1-\frac{c_{CO2,in}}{c_{CO2,ex}}}\right) \quad \mathbf{5}$$

The model operates on a crank angle resolved bases: the flow through the EGR valve will vary through the cycle as the driving pressure difference fluctuates. If independent flow characteristics of the valve can be obtained from a separate test facility or valve supplier, these could replace equation 6.

$$A_{valve,EGR} = f(\chi_{EGR}, N_{eng}) = a_4 + a_5\chi_{EGR} + a_6N_{eng} + a_7{\chi_{EGR}}^2 + a_8\chi_{EGR}N_{eng} + a_9{N_{eng}}^2 \quad \mathbf{6}$$

3.3 EGR cooler model

The EGR cooler was modelled using an effectiveness model (Equation 7) based on the inlet and outlet gas temperatures and the mean water temperature [32]:

$$T_{out} = T_{in-}\eta_{cooler}(T_{in} - T_{water}) \quad (7)$$

Cooler effectiveness (η_{cooler}) was calculated based on measured data and simplified to a quadratic equation calculating effectiveness as a function of flow rate through the cooler as shown in Figure 4. The resultant R^2 was poor 0.33, indicating a weak relationship between the two variables due to the large spread of deviation from the fit. The following factors can explain this:

- There is a measurement uncertainty for inlet air and coolant temperatures due to the positioning of the thermocouples. Further uncertainty in the measurement arises from the assumption of perfect mixing between fresh air and EGR gases which affects both the inlet manifold temperature and CO2 concentration measurement
- The model is particularly sensitive to its predicted EGR and exhaust flows because of the inherent feedback loop that the EGR leg introduces.

3.4 Cylinder model

A single zone model was chosen for the cylinder: this model treats the trapped volume inside the cylinder as a gas of homogeneous state which is most suited for real-time applications. The control volume for the cylinder varies in volume due to the cylinder kinematics as described in equation 8. Full details of the combustion model have previously been published by the authors in [33].

$$V_{cyl} = \frac{V_{dis}}{c-1} + \frac{\pi {D_{bore}}^2}{4}\left((r_{crank} + L_{con}) - \sqrt{{L_{con}}^2 - (r_{crank}\sin\theta)^2} - r_{crank}\cos\theta \right) \quad \mathbf{8}$$

Properties of the gas are assumed constant throughout the control volume and flow is allowed across the boundaries according to inlet and exhaust valve lifts, blow-by mass, and fuel injection.

The fuel injector used in this study uses a solenoid actuated valve which controls a "spill" flow of fuel through a control chamber back to the vehicle fuel tank. The spill flow creates a pressure imbalance on the injector needle causing the needle to rise, allowing flow through the nozzles into the cylinder. The main difficulty with this type of injector is determining when the injector needle is open as this cannot be deduced directly from an injector driver voltage or current. The total mass of fuel injected was determined as an empirical function of rail pressure, injector pulse duration and cylinder pressure from injector manufacturer data [34] and on-engine measurements [33] (see equation 9).

$$m_{f,pred} = a_{10}{m_{f,lookup}}^2 + a_{11}m_{f,lookup} - \left(a_{12}p_{cyl} + a_{13}\right) \quad 9$$

$$Where: m_{f,lookup} = f\left(t_{pulse}, p_{rail}\right),$$

The point at which the needle lifts and the injection begins (SOI) was determined by a full hydraulic model of the injector [35] and validated against measured high-frequency pressure fluctuations in

the fuel rail in proximity of the injector. This validation was achieved by assuming that the first pressure ripple in the crank angle resolved fuel pressure measurement, locating on the injector feed-pipe, corresponded to the lifting of the needle. Using both techniques, SOI was found to correspond to a point approximately 0.17ms into the injector current rise for all injections, pilot and main, and regardless of engine operating point. These results are consistent with those found by other authors [36].

The fuel flow rate into the cylinder at full needle lift was determined using Bernoulli flow (equation 10) with a discharge coefficient calculated with an empirical factor for cavitation (equation 11). The rail pressure was assumed to be a function of engine speed and load, but constant over an engine cycle such that the high frequency dynamics of the fuelling system were neglected.

$$\dot{m}_f = C_{d,noz}\rho_f A_{noz}\sqrt{\frac{2(p_{rail}-p_{cyl})}{\rho_f}} \quad 10$$

$$C_{d,noz} = C_c\sqrt{\frac{p_{rail}-p_{f,vap}}{p_{rail}-p_{cyl}}} \quad 11$$

The injector nozzle opening and closing was assumed to be instantaneous, meaning the nozzle area in equation 10 has a rectangular profile between the start and end of injection. The end of injection was determined using equation 12 where the total fuel mass to be injected is known in advance using equation 9. The injection model is applied sequentially to each individual injection event.

$$\int_{SOI}^{EOI} \dot{m}_f(t)dt = m_{f,pred} \quad 12$$

Blow-by was modelled using the analogy of an orifice connecting the cylinder with the crankcase (equation 13), where the flow coefficient was assumed to be constant with $\Psi = 0.532$. This approach has been shown to provide similar results when compared to variable flow coefficient models that better represented choking effects, but significantly reduce the calculation time for this model [37].

$$\dot{m}_{bb} = A_{bb} C_{d,bb} \frac{p_{cyl}}{\sqrt{RT_{cc}}} \psi \quad \mathbf{13}$$

The blow-by model was validated by calculating the total blow-by mass per cycle (equation 14 and comparing it to the measured blow by mass, calculated from a volumetric blow-by meter using equation 15.

$$m_{bb} = \int \dot{m}_{bb} dt \quad \mathbf{14}$$

$$m_{bb,meas} = \frac{\rho_{cc} \dot{V}_{bb,meas}}{2N_{eng}\, n_{cy}} \quad \mathbf{15}$$

Instantaneous temperature can be derived from the first law of thermodynamics (see equation 16 and Appendix B):

$$T_{cyl} = \int \frac{1}{m_{cyl} c_v} \left(\frac{dQ_{cyl}}{d\theta} - \frac{dQ_{ht}}{d\theta} - p_{cyl} \frac{d_{V_{cyl}}}{d\theta} + \frac{dm_{in}}{d\theta} h_{inl} - \frac{dm_{ex}}{d\theta} h_{cyl} - \frac{dm_{bb}}{d\theta} h_{cyl} \right) d\theta \quad \textbf{16}$$

And the instantaneous in-cylinder pressure can be found using the perfect gas law:

$$p_{cyl} = \frac{m_{cyl} R_{cyl} T_{cyl}}{V_{cyl}} \quad \textbf{17}$$

In-cylinder mass was calculating using the conservation of mass [9, 10] as shown in the following equation:

$$\frac{d_{m_{cyl}}}{d\theta} = \frac{dm_{in}}{d\theta} - \frac{dm_{ex}}{d\theta} + \frac{dm_f}{d\theta} - \frac{dm_{bb}}{d\theta} \quad \textbf{18}$$

Two critical parameters in equation 16 are the rate of heat release due to combustion and the heat transfer to the cylinder walls. Several techniques exist for accurately reproducing in-cylinder pressure and RoHR in an efficient way, including neural networks [38-41]; Wiebe methods (shape functions) [11, 32, 44, 47, 48]; however, in this work a mixing controlled combustion model was used [45-47].

The mixing controlled model is an extension of the combustion model originally proposed by Chemla [48]. It includes factors that improve the modelling of ignition delay, pre-mixed combustion, wall interaction and pilot combustion. The rate of fuel flow through the injector is also calculated from the solenoid control signal.

In this model, both physical and chemical ignition delays are considered according to the Magnussen and Arrinhius models (equations 19-21).

$$\int_{SOI}^{SOC} \frac{1}{\tau_{ID}} dt = 1, \;\; Where\; \tau_{ID} = \tau_{ph} + \tau_{ch} \qquad \textbf{19}$$

$$\frac{1}{\tau_{ch}} = C_{arr} c_f c_0 e^{-\frac{a_{14} T_{f,act}}{T_{cyl}}} \qquad \textbf{20}$$

$$\frac{1}{\tau_{ph}} = C_{mag} c_f \frac{\sqrt{k}}{\sqrt[3]{V_{cyl}}} \qquad \textbf{21}$$

$$\boldsymbol{where\; c_f = \frac{m_f}{V_{mix}}, \qquad c_o = \frac{0.232 m_{cyl}}{V_{mix}}}$$

The combustion process is split into two phases: a premixed combustion resulting from fuel build up in the cylinder prior to start of combustion and a diffusion controlled combustion. The premixed combustion (equation 22) heat release is calculated using the following terms:

- A term describing the reaction rate of the mixture

- An exponential term capturing the heating of the fuel
- The potential thermal energy available in injected fuel that is available from premixed combustion
- A quadratic term that captures the time elapsed since start of combustion to describe the initial burn rate.
- A final term to capture the dilution effect from the presence of EGR.

$$\frac{dQ_{pre}}{dt} = a_{15}\frac{\lambda \cdot AFR_{stoich}}{V_{mix}}\, e^{-a_{16}\frac{T_{f,act}}{T_{cyl}}}\, m_{pre,avail}^{2}\, LCV\, (t - t_{SOC})^{2}(1-\chi_{EGR})^{a_{17}} \quad \textbf{22}$$

In the diffusion model (equation 23), the combustion is calculated as a function of fuel availability, mixing rate, and a term to account for charge dilution with EGR. To model the effects of wall interaction, a parameter C_{wall} was used to model the effects of momentum being lost due to collision with the wall [49]. This factor is based on the estimation of flow penetration into the cylinder by considering the turbulent energy dissipation (equations 25 to 27)

$$\frac{dQ_{diff}}{dt} = C_{wall} \cdot C_{mod} \cdot LCV \cdot m_{f,diff,avail}\left(\frac{\sqrt{k}}{\sqrt[3]{V_{cyl}}}\right)(1-\chi_{EGR}) \quad \textbf{23}$$

The turbulent energy density was calculated with equation 24, which is a function of the cylinder energy E_{cyl}, resulting purely from the fuel injection process:

$$k = \frac{E_{cyl}}{m_f\left(1 + \lambda_{diff} AFR_{stoich}\right)} \quad 24$$

The rate of change in energy is defined as the difference between that input from fuel injection (E_i) and the energy dissipated (E_{diss}) [48]:

$$\frac{dE_{cyl}}{d\theta} = \frac{dE_i}{d\theta} - \frac{dE_{diss}}{d\theta} \quad 25$$

Energy input from the injection is described in equation 26, and the energy dissipation rate is described in equation 27.

$$\frac{dE_i}{d\theta} = C_{turb} 18 \rho_F \left(\frac{N_{eng}}{C_{d,noz} A_{noz}}\right)^2 \left(\frac{dm_f/d\theta}{\rho_f}\right)^3 \quad 26$$

$$\frac{dE_{diss}}{d\theta} = -\frac{C_{diss}}{6N_{eng}} E_{cyl} \quad 27$$

The heat transfer at the cylinder walls was modelled using equation 28, where h_c is the heat transfer coefficient calculated by a lumped heat transfer model as described in the following sections, combining convection and radiation using a known wall temperature $T_{cyl,wall}$.

$$\frac{dQ_{ht}}{d\theta} = h_{conv} A_{cyl}\left(T_{cyl,gas} - T_{cyl,wall}\right)\left(\frac{1}{6N_{eng}}\right) \quad \mathbf{28}$$

Although several heat transfer correlations are commonly used such as Woschni [30] and Hohenberg [50], a recent study by Finol [30] on a similar engine was used. The heat transfer coefficient is a

function of gas viscosity μ_{gas}, thermal conductivity k_{gas}, density, and mean piston speed as detailed in Equation 29:

$$h_{conv} = a_{18} B^{a_{19}-1} k_{gas} \left(\frac{a_{20} \rho_{gas} \bar{S}_p}{\mu_{gas}} \right)^{a_{19}} \quad \textbf{29}$$

The cylinder wall temperature was imposed based on measured values as a function of engine speed and percentage of maximum load.

3.5 Gas properties

A tri-gas species model was implemented that tracks the mass fractions of air (*a*), burnt gas products (*b*), and fuel (*f*) to calculate values of γ, u, and specific heats c_p, and c_v. Individual gas species' specific properties were obtained from [51]. The mass fraction of fuel was only considered in the cylinder as Diesel combustion efficiency is typically over 98% [29]. Outside of the cylinder, only the exhaust and air species were considered in gas property calculations as detailed in Appendix C. To find the mean gas properties, the mass weighted average of each property was calculated.

The exhaust manifold and EGR gas fractions are assumed to be equal to the in-cylinder gas fractions frozen at exhaust valve opening. Cylinder and inlet manifold gas fractions are updated continuously with the instantaneous flows in and out of their respective control volumes. Combustion events contribute towards to creation of exhaust gas within the cylinder as well as consuming air and fuel assuming stoichiometric combustion. Equations for the calculation of the gas fractions can be found

in Appendix C. In the cylinder, the specific gas constant was also calculated using equation 30 to account for cases with high rates of EGR.

$$R_{cv} = Y_a R_a + Y_b R_b + Y_f R_f \quad (30)$$

Where: $R_a = 287.05$ J/kgK [29], $R_f = 55.95$ J/kgK, $R_b = 285.4$ J/kgK [51]

4 Experimental Characterisation

The real-time model was parameterised for a 2.0L Turbocharged Diesel engine. The details of the engine hardware are summarised in Table 2. The engine was installed on an engine dynamometer facility.

Table 2 - Specification of the Ford 2.0L Engine installed at University of Bath

Parameter	Value
Engine Type	Turbocharged diesel
Cylinders	4
Capacity	1998cc
Stroke	86mm
Bore	86mm
Conrod Length	152mm
Firing Order	1-3-4-2
Compression Ratio	16 (using prototype pistons)
Max Torque	320Nm at 1800-2000rpm
Max Power	95kW at 3800rpm
Fuel Injection	Delphi common rail direct injection up to 1600bar

Two experimental configurations were used:

- Conventional fired engine tests
- Motored tests with varying intake manifold pressure and exhaust back pressure.

The fired engine tests covered the full engine speed/torque operating region, with and without EGR, and were measured using the standard engine configurations including turbocharger and full airpath. Figure 5 shows the ninety steady-state points covering the useful operating range of the test engine to characterise basic engine behaviour. Steady state points were taken at steps of 20Nm from 20Nm to the limiting torque curve (LTC) in steps of 500rev/min from 1000rev/min to 4000rev/min and in-cylinder data were averaged over 100 engine cycles. The region highlighted in grey shows the area where EGR measurements were taken. The EGR was varied in 5 steps up to the maximum achievable EGR rate whilst maintaining constant engine intake manifold pressure.

The motored tests were conducted using a boost pressure emulation system and exhaust back pressure valve [52]. The boost emulation configuration is shown schematically in Figure 6 which is used to control the intake manifold temperature and pressure. The system is supplied with cold 8bar air from a screw compressor and uses a series of valves and electric heater to adjust the pressure. The dump valve and water cooler are used to avoid excessive intake pressure in the case of engine stall and to allow transient control of the pressure. Motored tests were performed to improve the characterisation of the air path as effects due to combustion could be removed. However, with a standard engine configuration it is not possible to maintain representative cylinder pressures without engine firing because the turbocharger is starved of energy and cannot provide representative boost

pressures. The use of the boost emulation system overcomes this shortfall and it is possible to maintain representative intake manifold pressures without engine firing. Figure 7 shows how the intake manifold pressure was controlled across the speed range for motored tests. The standard engine conditions are also shown. The higher boost pressures allow peak in-cylinder pressure to be similar to firing conditions, even in the motored tests.

4.1 Instrumentation and measurements

The engine was monitored by two data acquisition systems: the first was a *CP Engineering Cadet Automation System* monitoring low frequency data at a rate of 20Hz and the second was a *D2T Osiris* system capturing indication data for every 0.1°CA. Table 3 summarizes the key instrumentation used in this study.

All measurements were taken after a warm-up for a period of 20 minutes at mid-speed, mid-load condition. At each point the engine was held for a settling period of 5 minutes before recording operating data over a period of 30 seconds and capturing 100 consecutive engine cycles at crank angle resolution. When undertaking measurements with EGR, this was increased to 300 cycles to cope with the increased cycle to cycle variability.

Table 3: Summary of key Instrumentation sensors

Low frequency	**CP Engineering Cadet Automation system**
Channel	**Sensor**
Fuel Flow	CP FMS1000 Gravimetric Flow Meter
Air Flow	ABB Sensy flow hot wire flow meter
Gas Pressure	Piezo-resistive pressure transducers
Gas Temperature	k-type thermocouple 1.5mm
Engine Torque	HBM analogue torque sensor
Emissions concentrations	Horiba Mexa 7000 Analyser

High Frequency	**D2T Osiris System**
Channel	**Sensor**
In-cylinder pressure	Kistler Piezoelectric Pressure Sensor (Type 6056A) installed in glow plug adaptor (Range 0-250bar)
Fuel rail pressure	Kistler Piezoelectric Pressure sensor (Type 4067A) installed on rail supply pipe (Range 0-2000bar).
Injector current	Picotech current clamp

The EGR fraction by mass was determined by two measurements of CO_2 volumetric concentration, the first taken in the exhaust flow ($CO_{2,exh}$)just after the turbocharger turbine and the second taken from the intake manifold ($CO_{2,inl}$).

4.2 Model Parameterisation

The model parameters were determined by minimising the sum squared error (SSE) between a measured and modelled value. This identification was performed sequentially on different parts of the model and with different optimisation targets. Five of the models were identified using all measured operating points as the models used in this work are highly empirical in nature.

1. The fuelling model was characterised using every measured point with firing conditions point from the Figure 5. The model parameters were identified to minimise the SSE between predicted and measured total fuel injected.
2. The exhaust manifold heat transfer parameters were optimised again using all measured data points under firing conditions and aimed to minimise the SSE between measured and modelled exhaust gas temperature at the turbocharger turbine entry
3. The EGR valve model parameters were identified by minimising SSE between modelled and measured EGR flow rates.
4. The EGR cooler effectiveness was identified based using measured and modelled intake manifold temperature.
5. The blow by model parameters were identified by comparing cycle averaged measured and modelled blow-by flow.

Different aspects of the combustion model were identified using carefully selected sub-sets of data [33].

1. Model constants for the ignition delay models were identified using data from a range of loads at constant engine speed of 2500rev/min (points a Figure 5). Parameter optimisation minimised the SSE between modelled and observed ignition delay.
2. The pre-mixed model constants identified by minimising SSE between the measured and modelled rate of heat release on a 0.1^{o}CA basis. Between inlet valve closing (IVC) and

exhaust valve opening (EVO). This was performed at a single, low speed and medium load operating point where pre-mixed combustion dominates (point c in Figure 5).

3. The diffusion model and pilot model were calibrated using the mid-speed, mid-load (point b in Figure 5), since at this load point the RoHR is mainly diffuse, and there is a pilot present prior to main injection. As with the pre-mixed model, the parameter identification optimisation sought to minimise the SSE between modelled and measured gross RoHR between IVC and EVO.
4. The Wall impingement parameter was identified after all other model parameters had been identified using a high speed and high load operating point (point d in Figure 5) and again the SSE of measured and modelled crank angle resolved RoHR was used as a minimisation target.

5 Model Validation

Individual sub-models were parameterised using different data sets to ensure the phenomena observed at different operating conditions were captured. The following sections summarise the performance of the model.

5.1 Airpath model validation

5.1.1 Motored operation

The filling and emptying model was initially validated against motored data. This data was taken at several speed and inlet manifold pressures. Indicated parameters (those measured once per cycle) were used to compare model data against measured data. Table 4 shows that overall, the filling and

emptying model performs very well with R^2 values over 0.94 for $p_{\max}$, net IMEP and mass airflow (MAF) prediction.

Table 4- Filling and emptying method prediction results

Parameter	R^2
p_{max}	0.971
Net IMEP	0.948
MAF	0.987

Figure 8 (a) shows how mass airflow increases with engine speed and increased inlet manifold pressure. Examining the mass airflow results in more detail, the model predicts the trend in mass airflow with varying speed and boost pressure closely, underestimating only slightly at high speed. This is thought to be due to the wave action and fluid momentum effects which have not been captured by the model [29].

Figure 8 (b) shows the model tends to under-predict peak pressure, except at low speed, where it is over-predicted. Additionally, the model over predicts the slight drop in peak pressure with increasing speed. As the inlet manifold pressure is increased, so does the error in predicted peak pressure; however, the error remains low and the overall trend is captured by the model.

Predicted net IMEP (including pumping loop) for the motored tests is compared in Figure 9 as contour plots. Both resulting contour plots show a similar trend. The model tends to under predict net IMEP with an error of approximately 0.2bar, particularly for low speed and boost.

5.1.2 Fired operation

The filling and emptying model was also validated against the fired map data and EGR map data. Figure 10(a) shows mass airflow at different engine speed and fuel demand points without EGR, with measured data indicated by crosses and model data indicated by red circles. This demonstrates that the model characterises mass airflow well across a wide range of engine operating conditions, indicating that it has captured both the trend and magnitude of mass airflow. Figure 10(b) shows modelled mass airflow plotted against measured mass airflow for both sets of data for all speed/load points. In both conditions the R^2 values were 0.99 indicating very high level of fit. This shows that the EGR valve model is highly predictive too, since mass airflow variation due to EGR set point is captured well over a range of speed and fuel demands.

Exhaust manifold heat transfer was validated by comparing measured exhaust manifold gas temperature against predicted temperature (Figure 11). The exhaust temperature is predominantly a function of the fuelling quantity and the poorest fits occur for the points at high torque and low engine speed. A similar conclusion was made for the points with EGR flow, with the model deteriorating only for high load and low speed conditions.

It is important to note that the errors may not be due solely to the filling and emptying model, since exhaust temperatures depend also on the combustion model. The combustion model assumes 100% combustion efficiency (a reasonable assumption under most normal operating conditions). The over-predicted temperatures at low mass airflow and high fuelling points can be accounted for due to

incomplete combustion. EGR rate would also have an influence on exhaust temperature due to the changes in inlet manifold temperature, combustion, and mass flow rate.

5.2 Combustion model validation

Prior to optimisation, the model already exhibited a reasonable representation of the trend in exhaust gas temperature as shown in Figure 12. Optimisation improved the prediction for both low and high loads, with a small level of error observed for medium load conditions and the final prediction statistics of the optimised model are shown in Table 5.

Table 5 – Comparison of model correlation coefficients (R^2) for RoHR data with EGR, and without EGR

Parameter	Without EGR	With EGR
p_{max}	0.989	0.946
$\theta_{max,RoHR}$	0.744	0.516
$\theta_{SOC,main}$	0.998	0.768
$RoHR_{max}$	0.961	0.323
$IMEP_{gross}$	0.996	0.990

6 Real Time Model

6.1 Model-wide improvements

To optimise execution time to meet the RT target, several areas of potential improvement were identified from the literature:

- Reduce the number of expensive blocks such as integrators, and blocks that contain pre-compiled code that cannot be optimised during code generation (S-blocks) [53]
- Reduce the number of power, exponential and trigonometric functions which use expensive Taylor series approximations during execution [12, 29]
- Enable in-lining of functions and parameters during code generation, which reduces the complexity of generated code and the number of global variables, thereby improving efficiency [21, 53]
- Design the simulation to be multi-rate, enabling processes outside the cylinder to be calculated at a lower resolution, thus saving on execution time [2, 12, 53].
- Use look-up tables or neural networks to replace expensive functions [11, 40]
- Hand-code specific optimised versions of complex functions [21]

Before any sub-model optimisations were undertaken, the model was arranged to calculate valve flow and in-cylinder conditions for only a single cylinder and duplicates this for multi-cylinder simulation. This reduced calculation time for valve flow, in-cylinder conditions and RoHR considerably, since the execution time penalty for modelling additional cylinders rises almost linearly

with each extra cylinder modelled. One key limitation of this is the inability to capture cylinder-to-cylinder variations that are most notably caused by uneven distribution of EGR. However, in a real time, the filling and emptying model assumes a homogeneous mixture of EGR and fresh air in the manifold, and therefore these effects cannot be captured. The approach also reduces the model's ability to predict cycle-to-cycle variations as it imposes four consecutive identical cycles.

Figure 13 shows how cylinder mass airflow and enthalpy were generated from a single modelled cylinder. This signal is then repeated with delays corresponding to the crank offset between cylinders (in this case 180^o for a four-cylinder engine). This delay had to be related back to engine speed, since this time reduces as the engine accelerates. Equation calculates the number of discrete time steps 31:

$$n_{delay} = \frac{\theta_{delay}}{6 N_{eng} t_{step}} \text{ , Where, } \theta_{delay} = 180, 360, 540 \ ^\circ CA \qquad \textbf{31}$$

Modelling multiple cylinders in this way did introduce some computational overhead as the inlet and exhaust flows need to be buffered so that the signal can be delayed and repeated for the other cylinders. Figure 14 shows how this method impacted on accuracy during a fixed speed load transient from around 30Nm to maximum torque. The inlet runner pressure rises steadily however a lag of up to one cycle is introduced in mass flow (since the other cylinders are back-calculated from the current cycle).

The model was also designed to use Euler integration (forward differencing). Although this method can be susceptible to instability and inaccuracy since it ignores second order terms, more complex, fixed step ODEs such as Runge-Kutta introduce large overheads and are unsuitable for running on an embedded systems [53].

Finally, floating point data were stored in single precision rather than double precision. This is because double precision numbers require twice the amount of memory compared to single precision numbers, and require twice the amount of clock cycles to process on 32-bit architecture [53], while single precision gives sufficient accuracy for this application.

The model was first run on a desktop PC using an Intel Core Duo processor at 3.16GHz. To measure total run-time, the models were first pre-complied using The Mathworks Matlab-Simulink accelerator mode, and then run five times to account for any variation due to other processes interrupting the simulation. Figure 15 shows box plots of the percentage run time per model, indicating the standard deviation by the size of the box, and the mean by the centre line.

6.2 Sub-model optimisation

The breakdown in Figure 15 showed that the most expensive sub-model was the rate of heat release calculation and this could offer the largest benefits. However, the model is capturing a complex process and ultimately little could be done to reduce this sub-model calculation times without reducing its fidelity.

The manifold sub-models run time was reduced by simplifying the valve flow approximation. This was achieved by exchanging the flow function equations with a single, two-dimensional look-up table in pressure ratio and gamma; reducing the number of expensive power operations contained in the flow function equation; and removing the need for logic deciding the flow regime and direction dependent on pressure ratio. To account for the severe non-linearity and the steepest aspect of the function being close to the change in flow direction, a dense look-up table was required. This look-up table density was optimised by analysing its run time vs. accuracy for different resolutions of pressure ratio indices. An example is shown in Figure 16 which shows that as the number of point in the lookup table is increased, the accuracy of the model increases (reduction in sum square errors – SSE). However, as the number of data point increases, the execution time of the model also increases. There exists an optimum point that can be determined by the modeller for each table.

The cylinder model also was improved by the valve look-up tables. The valve lift equations were collapsed into two look-up tables of effective area indexed by crank angle for each valve, depending on flow direction. This reduced the number of mathematical operations and look-ups performed for each timestep by a factor of three.

In the base model, cylinder volume and surface area calculations depend on several trigonometric functions, which are approximated using Taylor series during simulation. These were relatively expensive in terms of execution time and were converted into one-dimensional look-up tables, indexed by crank-angle.

Table 6 shows the improvement in execution time after the sub-model level optimisations were implemented. It shows that the biggest improvements gained were in the manifold and cylinder models. In total, a 28% improvement was observed between the original model and the optimised model, when comparing average accelerated run-times of the full model.

Table 6 – Percentage improvement in execution time of sub models after modifications (measured in accelerator mode on a desktop PC)

Sub model	RoHR	Manifolds	Cylinder	Volume	Heat Transfer	Total
Percentage run time improvement	<1%	38%	70%	20%	N/A	28%

6.3 Run time optimisation results

To approximate RT capability, the execution time was divided by the simulated time, assuming each timestep takes approximately the same amount of time to execute. The model was also benchmarked on the dSpace DS1006 board with an AMD Athlon processor at 1GHz. To determine the minimum timestep that the model would run real time, the timestep was then decreased stepwise until an overrun event was detected.

Before optimisation, the minimum timestep for the model to achieve real-time performance was 27.8µs which corresponded to a crank angle resolution of 0.66^{o}CA at 4000rpm. The optimisation of

the sub-models and the reductions in run time allowed the model time step to be reduced such that at 4000rpm engine speed, a crank angle resolution of 0.5°CA could be achieved. This is important because the crank angle resolution does influence the model accuracy. Figure 17 compared measured and modelled IMEP over a range of speeds for different resolutions. For both 0.1 and 0.2 °CA resolution, the results are largely the same, while at 0.5 °CA resolution there is a small offset, but still showing the same trend. At 1 °CA resolution, the simulation has lost a significant amount of accuracy, which is due to imprecision in injection timing, resulting in an offset in combustion timing and peak pressure.

6.4 Transient Validation of run time optimised model

Two sections of the new European drive cycle (NEDC) were simulated: the first urban phase of the cycle (UDC1) and the Extra urban phase (EUDC). Figure 18 illustrates these periods of the drive cycle. The cycle was design for a large passenger car application and the cycle was simulated and measured under fully hot conditions (with a 30min warm-up period to thermally soak the engine at operating temperature). Table 7 states the model to measured fit statistics for the UDC1 and EUDC phases of the drive cycle.

Table 7 –Correlation coefficients (R^2) for various model metrics over selected engine transients

Parameter	UDC 1			EUDC		
	R^2	RMSE	*RMSE %*	R^2	RMSE	RMSE %
Fresh air mass flow rate	0.98	0.0018kg/s	10%	0.99	0.0017kg/s	5.2%
Indicated mean effective pressure	0.93	0.6bar	28%	0.98	0.8bar	13%
Inlet manifold temperature	0.34	4K	1%	0.78	8K	2.3%
Exhaust manifold temperature	0.93	21K	4.2%	0.93	43K	6.7%
Peak cylinder pressure	0.90	4bar	8.6%	0.98	5.6bar	9.4%
Peak heat release	0.70	900J	55%	0.71	540J/CAD	23%
Peak cylinder temperature	0.87	82K	7.2%	0.89	140K	9.7%
Angle of peak cylinder pressure	0.64	4.7°	N/A	0.85	9.7°	N/A
Angle of peak heat release	0.23	103°	N/A	0.22	58°	N/A
Total heat released	0.93	62J	24%	0.98	80J	11%

The model performs better during the EUDC phase which sees higher engine loads and less gear shift events. The magnitude of the combustion processes is reasonably predicted (IMEP, peak pressure, peak heat release, total heat released), however the phasing of the combustion is less well captured (point of peak heat release and point of peak pressure). The inlet manifold temperature was predicted to within 10°C throughout the UDC and the EUDC. Despite this, the results in Table 7 suggest that the model yielded poor prediction of inlet manifold temperature during the UDC. This is because during the UDC, inlet manifold temperature varies over a small range compared to the EUDC, and although the model stays very close to the measured values, it swings between negative and positive error; whereas during the EUDC, inlet temperatures are nearly exclusively over-predicted by the model.

To allow for comparison of the measured and modelled temperature, the raw simulated temperature in the exhaust manifold was subjected to a first order filter. This is required because the

model can simulate temperature variations on a crank angle basis whereas the thermal mass of a thermocouple removes this level of detail for measurements. The exhaust temperatures were predicted to within 50°C of the measured temperature for both phases of the drive cycle.

Figure 19 details measured and modelled metric over the first acceleration of the EUDC to illustrate the results from Table 7. This shows the reasonable performance of the model in terms of IMEP, peak pressure, peak heat release and exhaust temperature.

7 Conclusions

A real time capable model of the core engine and combustion process has been presented. The model was composed of filling and emptying models representing the manifold and EGR legs and a mixing controlled combustion model. The model calculations are all performed on a crank angle basis giving a detailed prediction of in-cylinder pressure. As the model is built on physical equations, the model can be used for predicting behaviour and offers significant advantages over mean value engine models. The combustion model was parameterised using measured data from a small number of steady state operating points. The air path model was parameterised both using fired operation and a novel experimental approach with a motored engine and artificial boosting to maintain realistic operating conditions.

The parameterised models were first evaluated over the complete operating envelope of the engine including variations in EGR rate. During this process, the engine model yielded excellent prediction of mass airflow under fired and motored conditions with model and measurement matching with R^2

values of 0.99 in both cases. Cylinder filling behaviour was also validated by comparing peak motoring pressure and mean effective pressure to measured data; the model and measured data matched with an R^2 values of 0.97 and 0.94 respectively, indicating that the model matched engine performance over a range of engine speeds and boost pressures. The exhaust heat transfer model was also shown to give good prediction of exhaust temperatures over a range of speeds and loads, with and without the presence of EGR. The data with EGR gave a stronger agreement (R^2 of 0.92 compared to 0.82), but this was mainly due to the differences in engine speed/torque operating with and without EGR.

Run-time execution was improved by using forward differencing; single precision floating point numbers; and by only calculating in-cylinder prediction for a single cylinder. This was realised using a delay function which repeated the mass flow and enthalpy changes in the inlet and exhaust manifolds. A 25% improvement in RT run time was observed by applying sub-model level improvements. These were largely compromised of the strategic use of 1D/2D look-up tables in place of complex functions, combined with optimisation of the table resolution for accuracy/speed. The current model exceeds the performance of similar models in the literature achieving 0.5°CA resolution at 4000 rev/min. At the current resolution, the model still yields good accuracy compared to running at 0.1°CA resolution.

8 References

1. Benajes J, Lujan JM, Bermudez V and Serrano JR., *Modelling of turbocharged diesel engines in transient operation. Part 1: Insight into the relevant physical phenomena*, Proceedings of the

Institution of Mechanical Engineers, Part D: Journal of Automobile Engineering. 2002;216(5):431-41, DOI: 10.1243/0954407021529237

2. Schuette, H. and Ploeger, M., *Hardware-in-the-Loop Testing of Engine Control Units~A Technical Survey*, 2007, SAE International Warrendale Pennsylvania USA: Detroit, Michigan, SAE Paper Number 2007-01-0500
3. Kao M, Moskwa JJ, editors. *Turbocharged diesel engine modeling for nonlinear engine control and state estimation*, Proceedings of the 1993 ASME Winter Annual Meeting, November 28 - December 3, 1993; 1993; New Orleans, LA, USA: Publ by ASME
4. Jensen JP, Kristensen AF, Sorenson SC, Houbak N and Hendricks E., *Mean Value Modeling of a Small Turbocharged Diesel Engine*, SAE International Warrendale Pennsylvania USA: Detroit, Michigan, SAE Paper Number 910070
5. Müller M, Hendricks E and Sorenson SC., *Mean Value Modelling of Turbocharged Spark Ignition Engines*, 1998, SAE International Warrendale Pennsylvania USA: Detroit, Michigan, SAE Paper Number 980784
6. Fons M, Muller M, Chevalier A, Vigild C, Hendricks E and Sorenson SC., *Mean Value Engine Modelling of an SI Engine with EGR*, 1999, SAE International Warrendale Pennsylvania USA: Detroit, Michigan., SAE Paper Number 1999-01-0909
7. He Y and Lin C-C., *Development and Validation of a Mean Value Engine Model for Integrated Engine and Control System Simulation*, 2007, SAE International Warrendale Pennsylvania USA: Detroit, Michigan, SAE Paper Number 2007-01-1304

8. Rakopoulos CD and Giakoumis EG., *Review of Thermodynamic Diesel Engine Simulations under Transient Operating Conditions*, 2006, SAE International Warrendale Pennsylvania USA: Detroit, Michigan, SAE Paper Number 2006-01-0884
9. Zweiri, Y.H., Whidborne, J.F. and Seneviratne, L.D., *Dynamic simulation of a single-cylinder diesel engine including dynamometer modelling and friction*, Proceedings of the Institution of Mechanical Engineers Part D-Journal of Automobile Engineering, 1999. 213(D4): p. 391-402, DOI: 10.1243/0954407991526955
10. Black J, Eastwood PG, Tufail K, Winstanley T, Hardalupas Y and Taylor AMKP., *Diesel engine transient control and emissions response during a European Extra-Urban Drive Cycle (EUDC)*, 2007, SAE International Warrendale Pennsylvania USA: Kyoto, Japan, SAE Paper Number 2007-01-1938
11. Pacitti, G., Amphlett, S., Miller, P. Norris, R. and Truscott, A., *Real-Time, Crank-Resolved Engine Simulation for Testing New Engine Management Systems*, 2008, SAE International, Warrendale, Pennsylvania USA: Detroit, Michigan, SAE Paper Number 2008-01-1006
12. Schulze T, Wiedemeier M and Schuette H., *Crank Angle - Based Diesel Engine Modeling for Hardware-in-the-Loop Applications with In-Cylinder Pressure Sensors*, SAE International; 2007., DOI: 10.4271/2007-01-1303, SAE Paper Number 2007-01-1303
13. Nikzadfar K and Shamekhi AH., *An extended mean value model (EMVM) for control-oriented modeling of diesel engines transient performance and emissions*, Fuel. 2015;154:275-92, DOI: 10.1016/j.fuel.2015.03.070

14. Hendricks E and Sorenson SC., *Mean Value Modelling of Spark Ignition Engines*, 1990, SAE International Warrendale Pennsylvania USA: Detroit, Michigan, SAE Paper Number 900616
15. Maroteaux F and Saad C., *Combined mean value engine model and crank angle resolved in-cylinder modeling with NOx emissions model for real-time Diesel engine simulations at high engine speed*, Energy. 2015;88:515-27, DOI: 10.1016/j.energy.2015.05.072
16. Lee B and Jung D., *Thermodynamics-based mean-value engine model with main and pilot injection sensitivity*, Proceedings of the Institution of Mechanical Engineers, Part D: Journal of Automobile Engineering. 2016;230(13):1822-34, DOI: 10.1177/0954407015624525
17. Karlsson, J. and Fredriksson, J., *Cylinder-by-Cylinder Engine Models Vs Mean Value Engine Models for Use in Powertrain Control Applications*, SAE Technical Paper 1999-01-0906, 1999, doi:10.4271/1999-01-0906.
18. Schulten, P.J.M. and Stapersma, D., *Mean value modelling of the gas exchange of a 4-stroke diesel engine for use in powertrain applications*, 2003, SAE International Warrendale Pennsylvania USA: Detroit, Michigan, SAE Paper Number2003-01-0219
19. Hawley, J.G., Wallace, F.J. and Khalil-Arya, S., *A fully analytical treatment of heat release in diesel engines.* Proceedings of the Institution of Mechanical Engineers Part D-Journal of Automobile Engineering, 2003. **217**(D8): p. 701-717., DOI: 10.1243/09544070360692096
20. Chevalier A, Müller M and Hendricks E., *On the Validity of Mean Value Engine Models During Transient Operation*, 2000, SAE International Warrendale Pennsylvania USA: Detroit, Michigan, SAE Paper Number 2000-01-1261

21. Hunt G, Truscott A and Noble A., *An In-Cycle Hardware in the Loop (HiL) Simulator for Future Engine Control Strategy Development*, 2004, SAE International Warrendale Pennsylvania USA: Detroit, Michigan, SAE Paper Number 2004-01-0418
22. Watson, N. and Janota, M.S., *Turbocharging the Internal Combustion Engine*1982, London: The Macmillan Press LTD. ISBN 0-333-24290-4
23. Brace, C., *Transient Modelling of a DI TCi Diesel Engine*, 1996, PhD Thesis, in *Dept. Mechanical Engineering*, University of Bath: Bath.
24. Ganesh BM., *Hardware in the Loop Simulation (HIL) for Vehicle Electronics Systems Testing and Validation*, 2005, International Mobility Engineering Congress & Exposition 2005~SAE India Technology for Emerging Markets, India, SAE Paper Number 2005-26-304
25. Wurzenberger JC, Heinzle R, Schuemie A and Katrasnik T., *Crank-Angle Resolved Real-Time Engine Simulation –Integrated Simulation Tool Chain from Office to Testbed*, 2009, SAE International, Pennsylvania USA: Detroit, Michigan, SAE Paper Number 2009-01-0589
26. Wurzenberger JC, Bartsch P. and Katrasnik T., *Crank-Angle Resolved Real-Time Capable Engine and Vehicle Simulation - Fuel Consumption and Driving Performance*, 2010, SAE International Warrendale Pennsylvania USA: Detroit, Michigan, SAE Paper Number 2010-01-0784
27. Fiorani P, Gambarotta A, Tonetti M and Lanfranco E., *A Real-Time Model for the Simulation of Transient Behaviour of Automotive Diesel Engines*, 2006, SAE International, SAE Paper Number 2006-01-3007

28. Zweiri YH, Whidborne JF and Seneviratne LD., *Detailed analytical model of a single-cylinder diesel engine in the crank angle domain*, Proceedings of the Institution of Mechanical Engineers, Part D: Journal of Automobile Engineering. 2001;215(11):1197-216, DOI: 10.1243/0954407011528734
29. Heywood, J.B., *Internal Combustion Engine Fundamentals*1988, New York: McGraw-Hill, ISBN: 0-07-100499-8
30. Finol, C.F., *Heat transfer investigations in a modern Diesel engine*, PhD Thesis, 2008, Dept. of Mechanical Engineering, University of Bath, Bath
31. BSI. BS ISO 8178-1:2006, Reciprocating internal combustion engines. Exhaust emission measurement. Test-bed measurement of gaseous and particulate exhaust emissions. BSI; 2009.
32. Wiebe, I., *Habempirische Formel fur die Verbrennungsgeschrwindigkeit*, Verlag der Akademie der Wissenschaften der VdSSR, 1956, Moscow.
33. Dowell, P.G., Akehurst, S. and Burke, R.D., *An Improved Rate of Heat Release Model for Modern High Speed Diesel Engines*, 2016, ASME Paper Number ICEF2016-9630, Proceedings of the ASME 2016 Internal Combustion Engine Fall Conference, Oct. 9-12 2016, Greenville, SC, USA
34. Guerrassi, N. and Dupraz, P., *A common rail injection system for high-speed, direct-injection diesel engines*, SAE International Congress and Exposition, SAE International Warrendale Pennsylvania USA: Detroit, Michigan.

35. Dowell, P.D., *Real time heat release model of a HSDI Diesel engine*, PhD Thesis, 2012, Dept. of Mechanical Engineering, University of Bath, Bath
36. Van Alstine, D. G. Kocher, L.E., Koeberlein, E. and Shaver, G., *Control-Oriented Premixed Charge Compression Ignition Combustion Timing Model for a Diesel Engine Utilizing Flexible Intake Valve Modulation*, International Journal of Engine Research, vol. 14 no. 3 211-230, DOI: 10.1177/1468087412455606
37. Payri F, Molina S, Martin J and Armas O. *Influence of measurement errors and estimated parameters on combustion diagnosis*, Appl Therm Eng. 2006;26(2-3):226-36., DOI: 10.1016/j.applthermaleng.2005.05.006
38. He Y and Rutland CJ. *Application of artificial neural networks in engine modelling*, International Journal of Engine Research. 2004;5(4):281-96, DOI: 10.1243/146808704323224204
39. Longwic R., *Modelling the Combustion Process in the Diesel Engine with the Use of Neural Networks*, 2008., SAE Powertrains, Fuels and Lubricants Meeting, SAE International Warrendale Pennsylvania USA: Rosemont, Illinois, SAE Paper Number 2008-01-2446
40. Papadimitriou I, Silvestri J, Warner M and Despujols B., *Development of Real-Time Capable Engine Plant Models for use in HIL Systems*, 2008., SAE International Warrendale Pennsylvania USA: Detroit, Michigan, SAE Paper Number 2008-01-0990
41. Galindo J, Lujan JM, Serrano JR and Hernandez L., *Combustion simulation of turbocharger HSDI Diesel engines during transient operation using neural networks*, Appl Therm Eng. 2005;25(5-6):877-98, DOI: 10.1016/j.applthermaleng.2004.08.004

42. Watson N, Pilley AD and Marzouk M., *A Combustion Correlation for Diesel Engine Simulation*, 1980, SAE International Warrendale Pennsylvania USA: Detroit, Michigan, SAE Paper Number 800029

43. Miyamoto N, Chikahisa T, Murayama T and Sawyer R. *Description and Analysis of Diesel Engine Rate of Combustion and Performance Using Wiebe's Functions*. SAE International; 1985, SAE Paper Number 850107

44. Friedrich I and Pucher H, *Offer T. Automatic Model Calibration for Engine-Process Simulation with Heat-Release Prediction*, SAE International; 2006, SAE Paper Number 2006-01-0655

45. Pirker G, Chmela F and Wimmer A., *ROHR Simulation for DI Diesel Engines Based on Sequential Combustion Mechanisms*, SAE International; 2006, SAE Paper Number 2006-01-0654

46. Arregle J, Lopez JJ, Garcia JM and Fenollosa C., *Development of a zero-dimensional Diesel combustion model: Part 2: Analysis of the transient initial and final diffusion combustion phases*, Appl Therm Eng. 2003;23(11):1319-31. DOI: 10.1016/S1359-4311(03)00080-2

47. Arregle J, Lopez JJ, Garcia JM and Fenollosa C., *Development of a zero-dimensional Diesel combustion model. Part 1: Analysis of the quasi-steady diffusion combustion phase*, Appl Therm Eng. 2003;23(11):1301-17. DOI: 10.1016/S1359-4311(03)00079-6

48. Chmela, F.G. and Orthaber, G.C., *Rate of heat release prediction for direct injection diesel engines based on purely mixing controlled combustion*, SAE International Warrendale Pennsylvania USA: Detroit, Michigan, SAE Paper Number 1999-01-0186

49. Lakshminarayanan, P.A., Aghav, Y.V., Dani, A.D. and Mehta, P.S., *Accurate prediction of the rate of heat release in a modern direct injection diesel engine*, Proceedings of the Institution of Mechanical Engineers Part D-Journal of Automobile Engineering, 2002. 216(D8): p. 663-675, DOI: 10.1177/095440700221600805
50. Hohenberg GF., *Advanced Approaches for Heat Transfer Calculations*. SAE International; 1979, SAE Paper Number 790825
51. Lapuerta M, Armas O and Hernandez JJ., *Diagnosis of DI Diesel combustion from in-cylinder pressure signal by estimation of mean thermodynamic properties of the gas*, Appl Therm Eng. 1999;19(5):513-29, DOI: 10.1016/S1359-4311(98)00075-1
52. Zhang, K., *Air Charge Emulation for Diesel Engine*, PhD Thesis, Department of Mechanical Engineering, University of Bath, UK, 2010
53. Anon, *Real-Time Workshop Embedded Coder for Production Code Generation* 2010: Mathworks.
54. Y.A., C. and B. M.A., *Thermodynamics an Engineering Approach*. 3rd ed1998, New York: McGraw-Hill.

9 Notation

A		m^2
a_{1-}	Fitted Constants	-
AFR_{stoich}	Stoichiometric air fuel ratio	-
c	Compression ratio	-

C_{arr}	Arrhenius model constant (Fitted)	-
C_c	Fuel injector cavitation coefficient	-
C_d	Discharge coefficient	-
C_{diss}	Cylinder turbulent energy dissipation factor	-
C_{mag}	Magnussen model constant (Fitted)	-
C_{mod}	Chemla diffusion Combustion model constant (fitted)	J/kg ^{o}CA
c_p	Specific heat at constant pressure	J/kgK
C_{turb}	Injection turbulent energy factor	-
c_v	Specific heat at constant volume	J/kgK
C_{wall}	Model parameter to account for wall impingement	-
D	Characteristic Length	m
E	Cylinder turbulent energy	J
h_{conv}	Convective heat transfer coefficient	W/m^{2}K
h	Specific enthalpy	J/kg
k	Thermal conductivity, Turbulence density	W/mK, m^2/s^2
L	Length	m

L_f	Latent heat of vaporisation of fuel	J/kg
m	Mass	kg
$m_{f,lookup}$	Total mass of fuel injected per injection event from injector characteristics	kg
$m_{f,pred}$	Predicted total mass of fuel injected into cylinder per injection event	kg
N_{eng}	Engine rotational speed	rev/min
n_{cy}	Number of Cylinders	
p	Pressure	Pa
Pr	Prandtl Number	-
Q	Heat transfer	J
R^2	Coefficient of determination	-
R	Gas Constant	J/kgK
r	Radius	m
Re	Reynolds number	-
$\bar{S}_p$	Mean piston Speed	m/s
T	Temperature	K
t	Time	s
t_{pulse}	Injector signal pulse width	s
U	Internal Energy	J
u	Specific internal energy	J/kg

V	Volume	m^3
W	Mechanical Work	J
w_{seat}	Valve seat width	
Y	Mass fraction	-
β	Valve seat angle	rad
γ	Ratio of specific heats	-
δ_{os}	Piston pin offset	m
η_{cooler}	Heat exchanger effectiveness	-
θ	Crank Angle	^{o}
λ	Stoichiometric ratio for premixed combustion	-
λ_{diff}	Stoichiometric ratio of the diffusion flame	-
μ	Dynamic Viscosity	kg/ms
ρ	Density	kg/m^3
τ	Ignition delay parameter	-
ϕ	Con rod angle when piston is at TDC	rad
χ_{EGR}	EGR rate by mass	-
Ψ	Flow Function	-

a	Fresh Air
act	Activation (temperature)

$avail$	Available fuel
b	Burnt gases
bb	Blow by
$bore$	Cylinder bore
cc	Crank Case
cyl	Cylinder
con	Con rod
$crank$	Crank level arm
$diff$	Diffusive combustion
dis	Displacement
ex	Exhaust valve
exh	Exhaust Manifold
f	Fuel
ht	Heat Transfer
i	Control volume index
inl	Inlet manifold
in	Inlet Valve
noz	Fuel injector nozzle
pre	Pre-mixed combustion
$rail$	High Pressure Fuel Rail
soc	Start of combustion
vap	Vaporization
$wall$	Wall (temperature)

CR	Compression Ratio
ECU	Engine Control Unit
EGR	Exhaust Gas Recirculation
EVO	Exhaust Valve Opening
HiL	Hardware in the Loop
IMEP	Indicated Mean effective pressure
IVC	Inlet Valve Closing
LTC	Limiting Torque Curve
MAF	Mass Air Flow
MVEM	Mean Value Engine Model
ODE	Ordinary Differential Equation
pmax	Maximum In cylinder pressure
RDE	Real Driving Emissions Legislation
RMSE	Root Mean Square Error
RoHR	Rate of Heat Release
RT	Real Time
VGT	Variable Geometry Turbocharger
WLTC	World Harmonized Light Duty Cycle

10 Appendix

A1 Valve flow equations

The flow function can be derived as a function of inlet and outlet pressures (stations 1 and 2 respectively) and gamma [29]:

$$\Psi = \begin{cases} \left(\frac{2}{\gamma+1}\right)^{\frac{1}{\gamma-1}}\sqrt{\frac{2\gamma}{\gamma+1}} & 0 < \frac{p_2}{p_1} < \left(\frac{2}{\gamma+1}\right)^{\frac{1}{\gamma-1}} \\ \sqrt{\left(\frac{2\gamma}{\gamma-1}\right)\left[\left(\frac{p_2}{p_1}\right)^{2/\gamma} - \left(\frac{p_2}{p_1}\right)^{\frac{\gamma+1}{\gamma}}\right]} & \left(\frac{2}{\gamma+1}\right)^{\frac{1}{\gamma-1}} < \frac{p_2}{p_1} < 1 \\ -\sqrt{\left(\frac{2\gamma}{\gamma-1}\right)\left[\left(\frac{p_1}{p_2}\right)^{2/\gamma} - \left(\frac{p_1}{p_2}\right)^{\frac{\gamma+1}{\gamma}}\right]} & 1 < \frac{p_2}{p_1} < \left(\frac{2}{\gamma+1}\right)^{-\frac{1}{\gamma-1}} \\ -\left(\frac{2}{\gamma+1}\right)^{\frac{1}{\gamma-1}}\sqrt{\frac{2\gamma}{\gamma+1}} & \left(\frac{2}{\gamma+1}\right)^{-\frac{1}{\gamma-1}} \le \frac{p_2}{p_1} \end{cases} \quad \textbf{32}$$

Valve area with respect to valve lift is described by the following equation [10]:

$$A_{Valve} = \begin{cases} \pi L_{valve}\cos\beta\left(D_{valve} - 2w_{seat} + \frac{L_{valve}}{2}\sin 2\beta\right) & L_{low} \ge L_{valve} > 0 \\ \pi\left(D_{seat} - w_{seat}\right)\sqrt{\left(L_{valve} - w_{valve}\tan\beta\right)^2 + w_{valve}^2} & L_{high} \ge L_{valve} > L_{low} \\ \frac{\pi}{4}\left(D_{port}^2 - D_{seat}^2\right) & L_{valve} > L_{high} \end{cases} \quad \textbf{33}$$

Where: $L_{low} = \frac{w_{seat}}{\sin\beta \cdot \cos\beta}$, $L_{high} = \sqrt{\left(\frac{D_{port}^2 - D_{seat}^2}{4\{D_{seat} - w_{seat}\}}\right)} + w_{seat}\tan 2\beta$

Figure 20 illustrates the flows and evolution of mass in the cylinder control volume over a complete engine cycle. The inlet valve opens during a short valve overlap period where inlet valve area is proportional to inlet valve lift. A small amount of backflow is observed due to high exhaust backpressure before valve area approaches its maximum and cylinder filling begins. After the valve area starts to decrease, the mass flow decreases prior to inlet valve close (IVC) at -120°CA after top dead centre (ATDC). Around top dead centre (TDC), a small amount of trapped mass is lost through blow-by before exhaust valve open (EVO) at 120 °CA ATDC. Valve flow is minimal until the exhaust valve area rises to its maximum and blow-down begins. Cylinder mass continues to drop until the valve overlap period, leaving a small amount of residual gas remaining.

A2 In-cylinder calculations

Considering a single zone combustion models shown in the system shown in Figure 21

Applying the first law of thermodynamics and solving numerically in the crank angle domain yields Equation 34 [29].

$$\frac{dU_{cyl}}{d\theta} = \frac{dQ_{cyl}}{d\theta} - \frac{dW_p}{d\theta} - \frac{dQ_{ht}}{d\theta} + \frac{dm_{inl}}{d\theta}h_{inl} - \frac{dm_{exh}}{d\theta}h_{exh} + \frac{dm_f}{d\theta}h_f - \frac{dm_{f,v}}{d\theta}L_f - \frac{dm_{bb}}{d\theta}h_{cyl} + \sum_i dm_{i,cyl}u_i \quad \textbf{34}$$

By considering the gas to be perfect, the work done on the gas by the piston per °CA is:

$$\frac{dW_p}{d\theta} = p_{cyl}\frac{dV_{cyl}}{d\theta} \quad \textbf{35}$$

Furthermore, the internal energy can be defined as:

$$u_{cyl} = m_{cyl}c_v\frac{dT_{cyl}}{d\theta} \text{ Assuming: } \frac{dm_f}{d\theta}h_f \approx 0 \text{ and } \frac{dm_{f,v}}{d\theta}L_f \approx 0 \quad \textbf{36}$$

This gives results in Equation 37:

$$m_{cyl}c_v\frac{dT_{cyl}}{d\theta} = \frac{dQ_{cyl}}{d\theta} - \frac{dQ_{ht}}{d\theta} - p_{cyl}\frac{dV_{cyl}}{d\theta} + \frac{dm_{inl}}{d\theta}h_{inl} - \frac{dm_{exh}}{d\theta}h_{exh} - \frac{dm_{bb}}{d\theta}h_{cyl} \quad \textbf{37}$$

Equation 37 can be solved for temperature by integrating with respect to ^{o}CA:

$$T_{cyl} = \int \frac{1}{m_{cyl}c_v}\left(\frac{dQ_{cyl}}{d\theta} - \frac{dQ_{ht}}{d\theta} - p_{cyl}\frac{dV_{cyl}}{d\theta} + \frac{dm_{inl}}{d\theta}h_{inl} - \frac{dm_{exh}}{d\theta}h_{exh} - \frac{dm_{bb}}{d\theta}h_{cyl}\right)d\theta \quad \textbf{38}$$

Volume can be described by the motion of the piston-crank mechanism [28]:

$$V_{cyl} = \frac{V_{dis}}{c-1} + \frac{\pi D_{bore}^{\ 2}}{4}\left\{\sqrt{\left(r_{crank}+L_{con}\right)^2 - \delta_{os}^{\ 2}} - \sqrt{L_{con}^{\ 2} - \left[\delta_{os} + r_{crank}\sin\left(\theta-\phi\right)\right]^2} - r_{crank}\cos\left(\theta-\phi\right)\right\} \quad \textbf{39}$$

$$\frac{dV_{cyl}}{d\theta} = \left\{\sin\left(\theta-\phi\right) + \frac{\cos\left(\theta-\phi\right)\left[\delta_{os} + r_{crank}\sin\left(\theta-\phi\right)\right]}{\sqrt{L_{con}^{\ 2} - \left[\delta_{os} + r_{crank}\sin\left(\theta-\phi\right)\right]^2}}\right\} \text{ Where, } V_{dis} = 2r_{crank}\frac{\pi D_{bore}^{\ 2}}{4} \quad \textbf{40}$$

Since the piston-pin offset, δ_{os}, and ϕ are zero, this expression can be simplified to:

$$V_{cyl} = \frac{V_{dis}}{c-1} + \frac{\pi D_{bore}^{\ 2}}{4}\left\{\left(r_{crank}+L_{con}\right) - \sqrt{L_{con}^{\ 2} - \left[r_{crank}\sin\left(\theta\right)\right]^2} - r_{crank}\cos\left(\theta\right)\right\} \quad \textbf{41}$$

$$\frac{dV_{cyl}}{d\theta} = \left\{ \sin(\theta) + \frac{\cos(\theta)[r_{crank}\sin(\theta)]}{\sqrt{L_{con}{}^2 - [r_{crank}\sin(\theta)]^2}} \right\} \quad \textbf{42}$$

A3 Gas properties equations

Individual gas fraction properties were calculated using the following equations:

$$c_{V,a} = -10.4199 \cdot T^{0.5} + 2522.88 - 67227.1 \cdot T^{-0.5} + 917124.4 \cdot T^{-1} - 4174853.6 \cdot T^{-1.5} \quad \textbf{43}$$

$$c_{V,f} = -200.447 + 6.95372 \cdot T - (4.04715 \cdot 10^{-3}) \cdot T^2 + (9.10259 \cdot 10^{-7}) \cdot T^3 + 1458487 \cdot T^{-2} \quad \textbf{44}$$

$$c_{V,b} = 641.154 + 0.43045 \cdot T - 0.0001125 \cdot T^2 + (8.979 \cdot 10^{-9}) \cdot T^3 \quad \textbf{45}$$

$$u_a = -4193697.9 - 6.9466 \cdot T^{1.5} + 2522.88 \cdot T - 134454.16 \cdot T^{0.5} + 917124.39 \cdot \log(T) + 8349707.14 \cdot T^{-0.5} \quad \textbf{46}$$

$$u_f = -1445686.1 - 200.447 \cdot T + 3.47686 \cdot T^2 - (1.34905 \cdot 10^{-3}) \cdot T^3 + (2.27565 \cdot 10^{-7}) \cdot T^4 - 1458487 \cdot T^{-1} \quad \textbf{47}$$

$$u_b = -3251495 + 1028.75 \cdot T - 0.15377 \cdot T^2 + (6.789 \cdot 10^{-5}) \cdot T^3 \quad \textbf{48}$$

Further gas properties including enthalpy h can be derived from the above values [54]:

$$h_a = u_a + R_a \cdot T \quad \textbf{49} \qquad c_{P,a} = c_{V,a} + R_a \quad \textbf{50} \qquad \gamma_a = {c_{P,a}}/{c_{V,a}} \quad \textbf{51}$$

$$h_f = u_f + R_f \cdot T \quad \textbf{52} \qquad c_{P,f} = c_{V,f} + R_f \quad \textbf{53} \qquad \gamma_a = {c_{P,f}}/{c_{V,f}} \quad \textbf{54}$$

$$h_b = u_b + R_b \cdot T \quad \textbf{55} \qquad c_{P,b} = c_{V,b} + R_b \quad \textbf{56} \qquad \gamma_a = {c_{P,b}}/{c_{V,b}} \quad \textbf{57}$$

To find the mean gas properties, the average of each property was taken, weighted by the mass fraction of each gas species.

A4 List of Empirical Model Parameters

Equation	Parameter	Value	Unit
2	a_1	-0.056	K/g^2
	a_2	6.4	K/g
	a_3	384	K
4	a_4	4.59×10^{-7}	m^2
	a_5	2.282×10^{-5}	m^2/mmEGR
	a_6	1.296×10^{-8}	m^2/rpm
	a_7	3.092×10^{-7}	m^2/mmEGR^2
	a_8	3.978×10^{-9}	m^2/(mmEGR rpm)
	a_9	3.292×10^{-12}	m^2/rpm^2
7	a_{10}	-0.0042	g/g^2
	a_{11}	1.2731	g/g

	a_{12}	-0.0357	g/Pa
	a_{13}	3.963	g
8	A_{noz}	10.62 x 10^{-8}	m^2
9	C_c	0.7	
11	A_{bb}	2.64 x10^{-7}	m^2
	$C_{d,bb}$	0.53	
18	C_{arr}	128.2 (pilot) 48 (main)	
	a_{14}	2.664 (pilot) 2.542 (main)	
	$T_{f,act}$	1000	K
19	C_{mag}	10.26 (pilot) 26.1 (main)	
20	a_{15}	0.5 x10^{12}	
	a_{16}	1 x 10^{-3}	
	a_{17}	1	
21	C_{mod}	0.9	
24	C_{turb}	1	
25	C_{diss}	100	
27	a_{18}	0.0975	
	a_{19}	0.8	
	a_{20}	1.5	

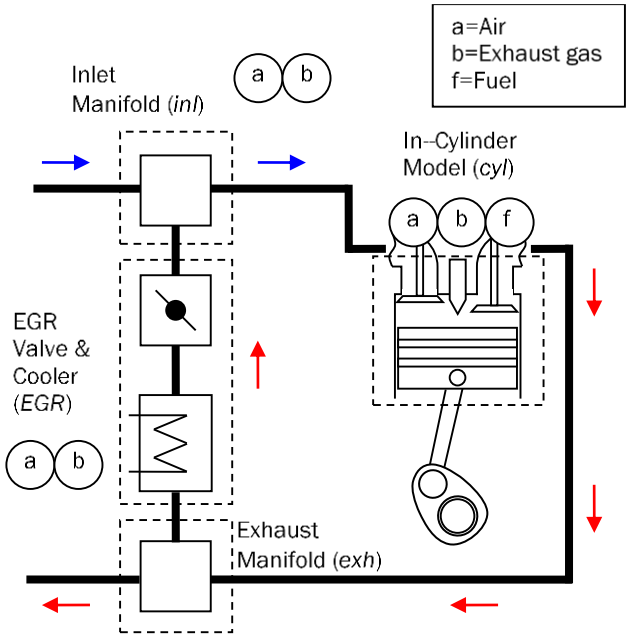

Figure 1- Airpath model schematic indicating sub-models and flow direction

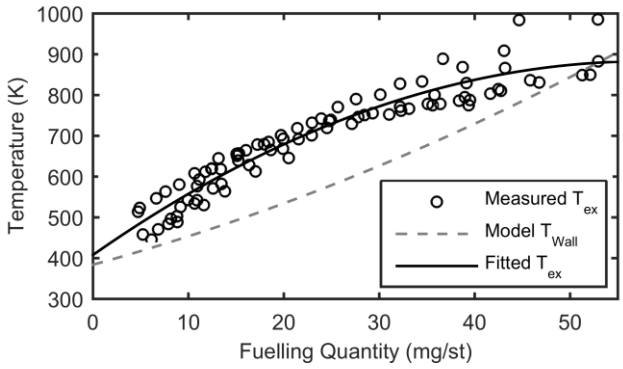

Figure 2 - Exhaust manifold gas temperature trend with fuel demand

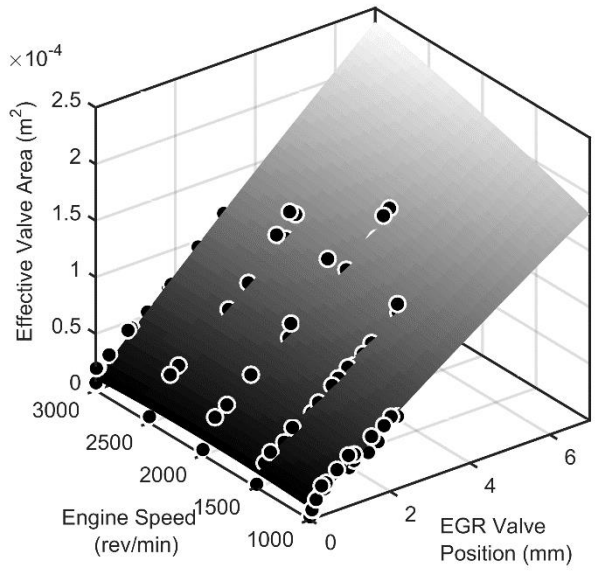

Figure 3 - EGR effective area map

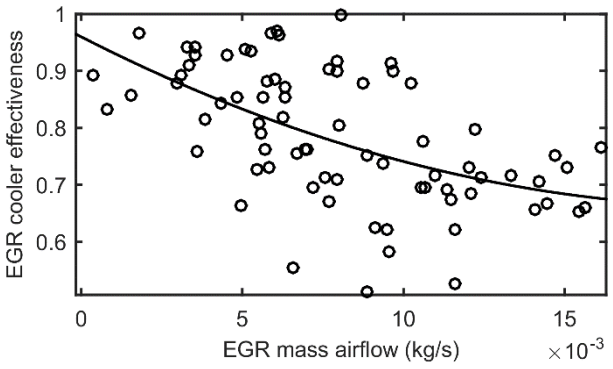

Figure 4 - EGR cooler effectiveness model based on EGR mass airflow

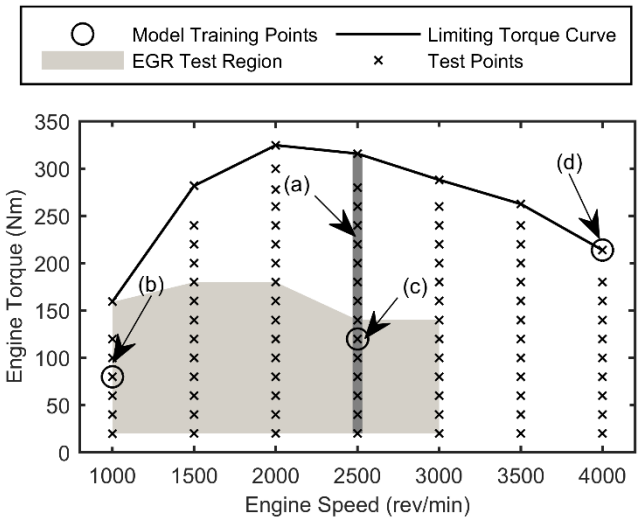

Figure 5 - Engine map speed/ torque test points LTC=limiting torque curve

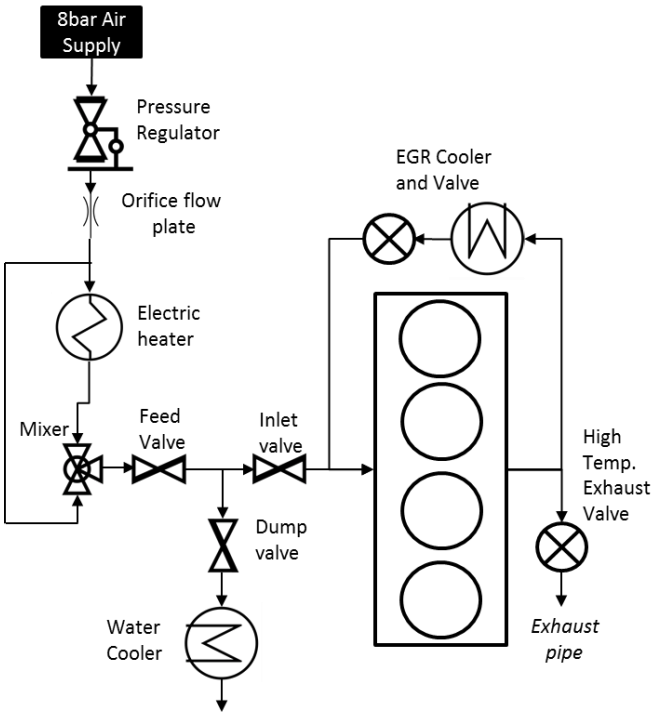

Figure 6: Engine air path layout with boost emulation facility

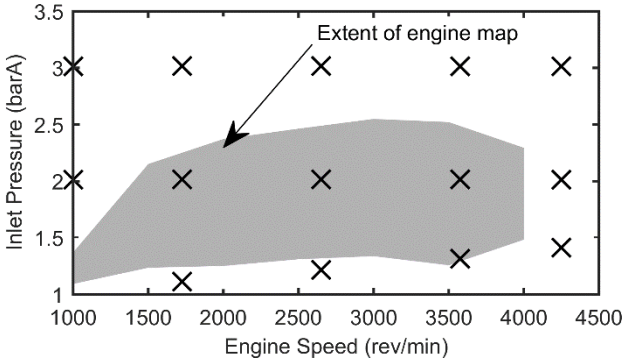

Figure 7 - Motored map speed / inlet manifold pressure test points

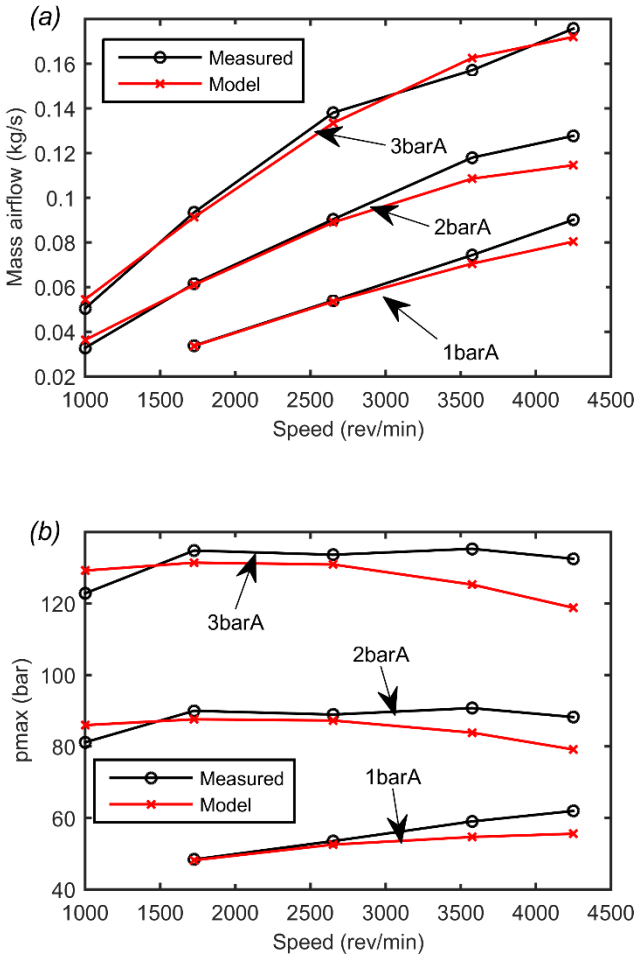

Figure 8 - Comparison between measured and simulated results for (a) mass airflow and (b) p_{max} under motored conditions

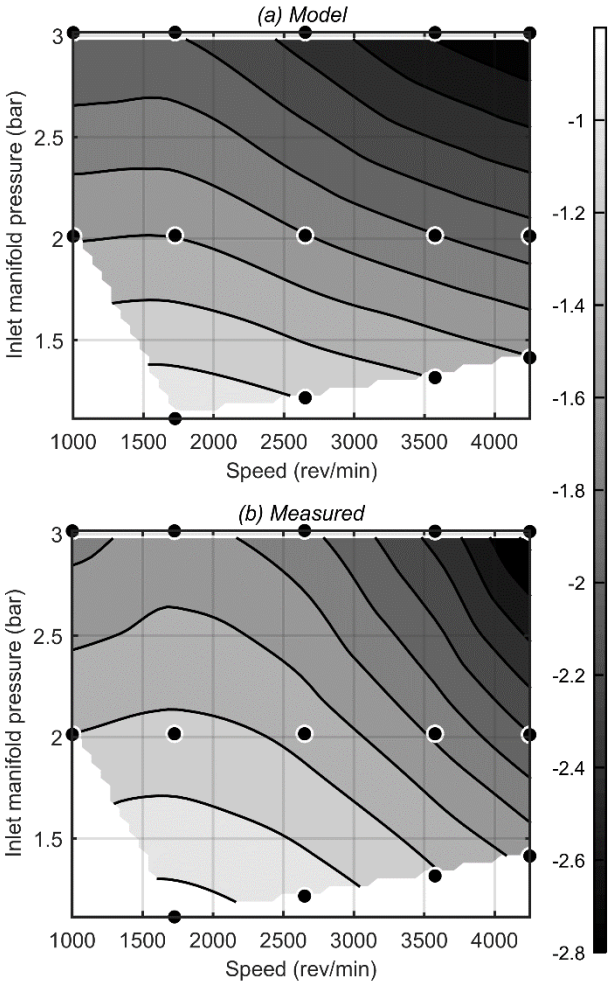

Figure 9 –quadratic surface fits (contours) of nIMEP data (circles) generated by simulation compared against measured data

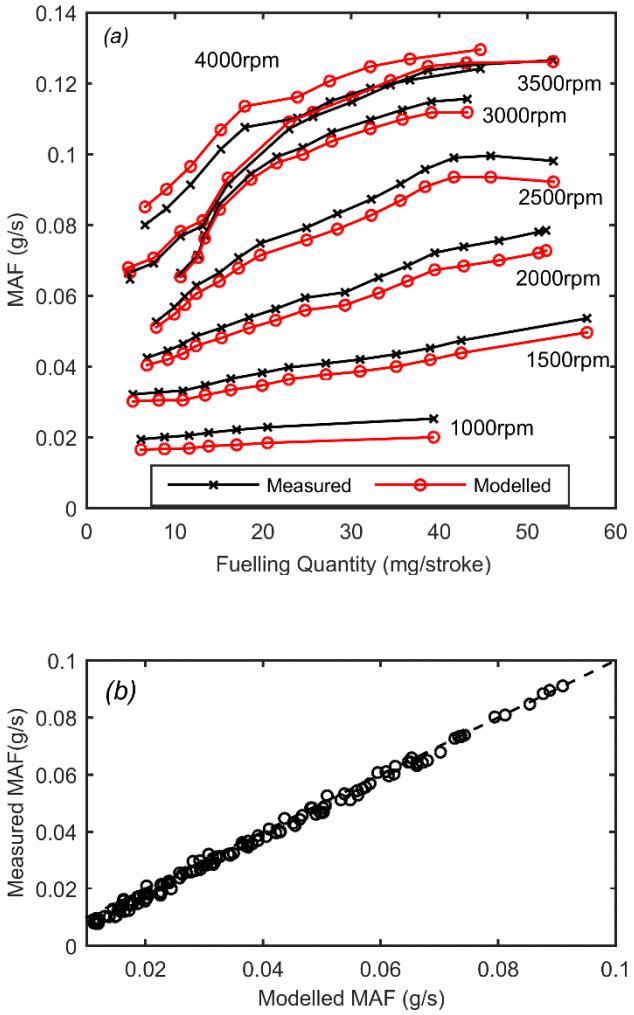

Figure 10 - Fired map data mass airflow prediction (a) without EGR and (b) with EGR

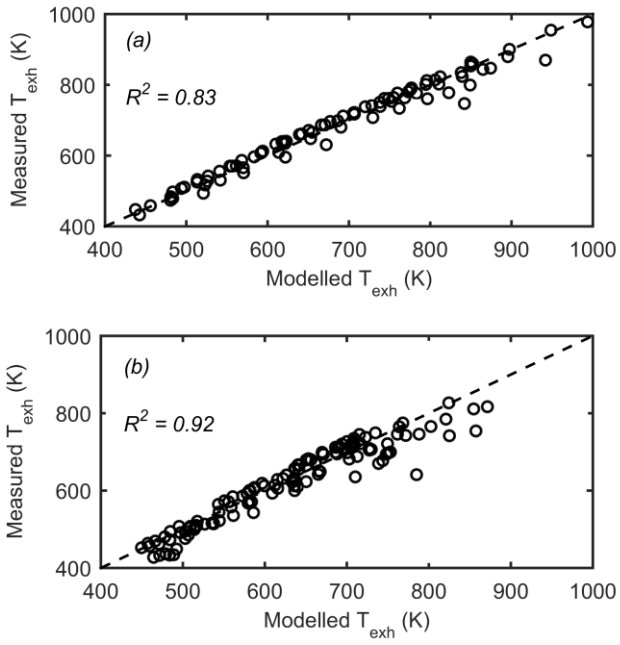

Figure 11 – Predicted vs. measured exhaust temperature from: (a) Fired map data and, (b) EGR map data

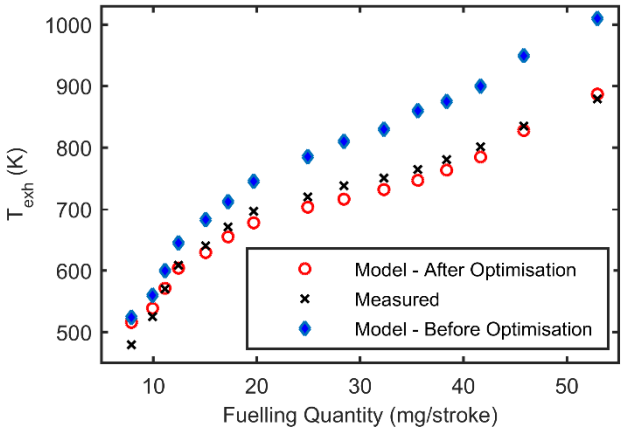

Figure 12 - Optimised model at 2500rev/min

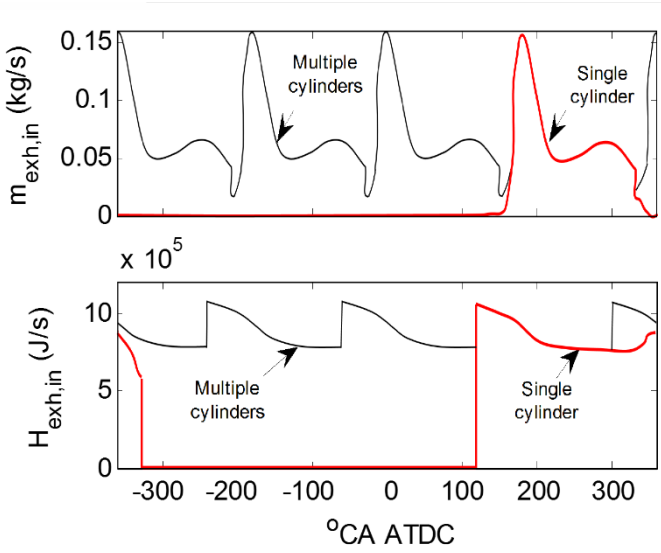

Figure 13 - Single cylinder to multi-cylinder transform

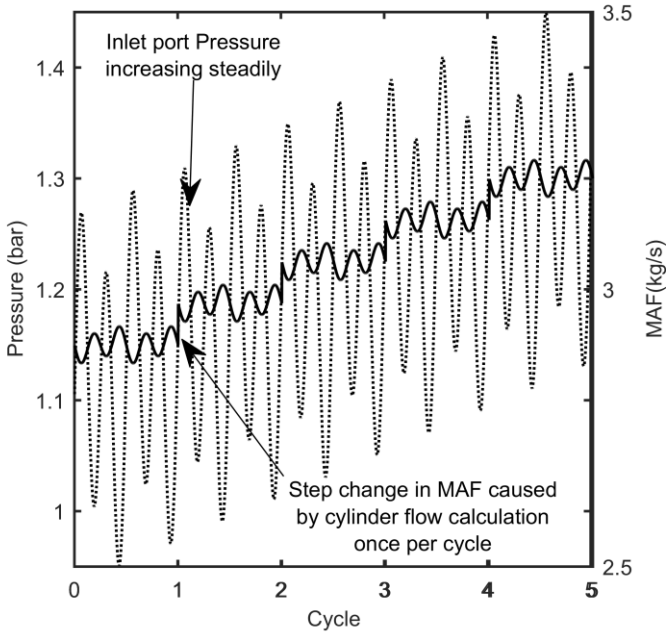

Figure 14 - Loss of cylinder flow resolution due to emulation of 4 cylinders from a single cylinder

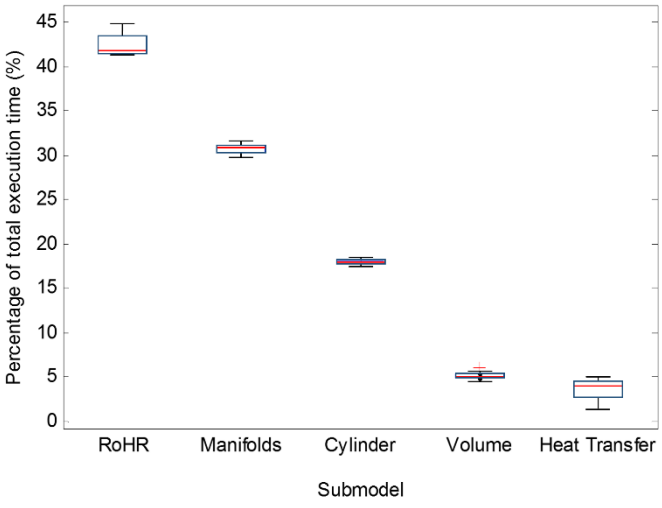

Figure 15 - Percentage execution time of each sub-model

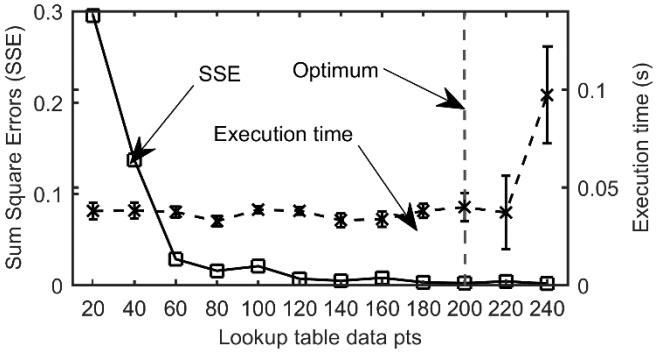

Figure 16: Example of lookup table optimisation.

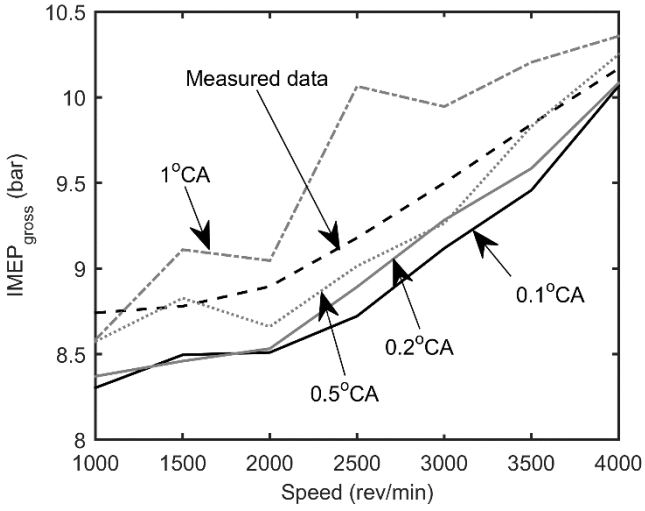

Figure 17 - IMEP prediction at 50% load and increasing speeds for different CA resolutions at4000rev/min

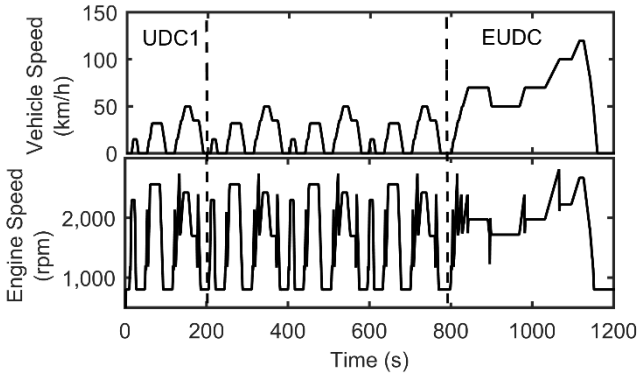

Figure 18 – NEDC drive cycle highlighting periods for which model performance statictics have been computed

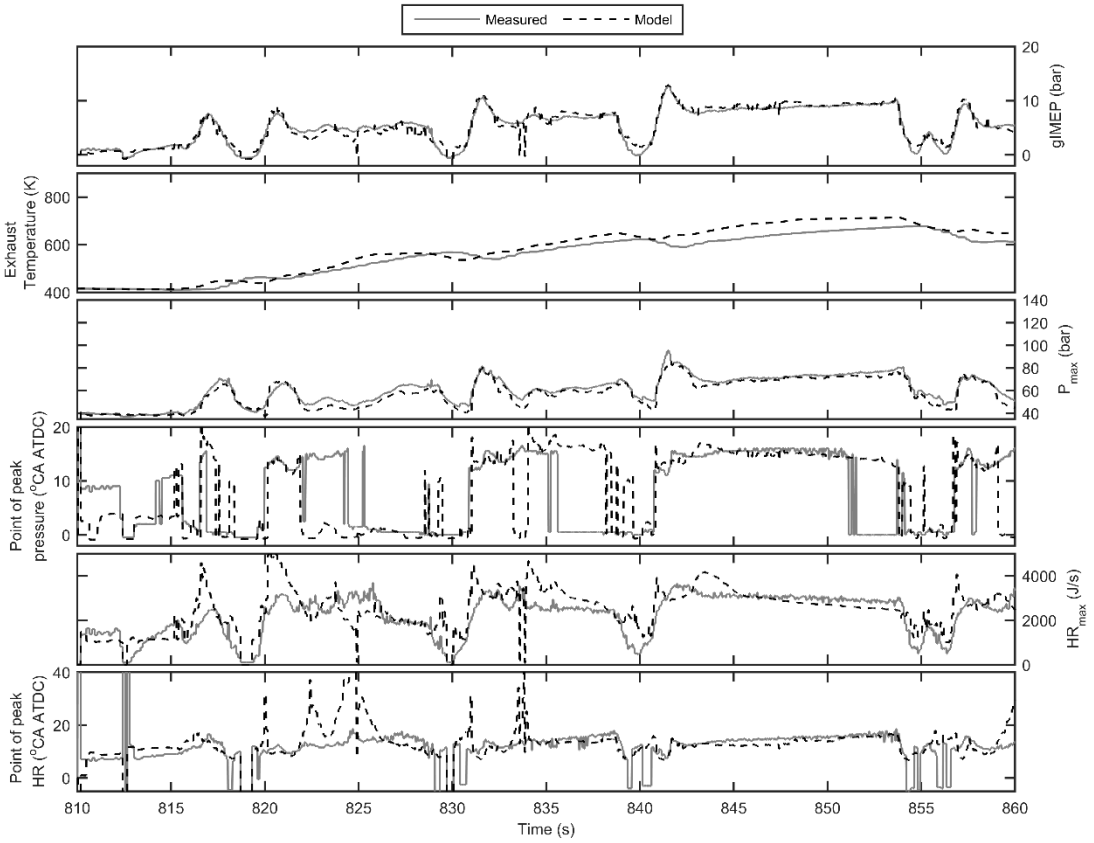

Figure 19 – Comparison of model and measured IMEP, exhaust temperature, peak pressure, point of peak pressure, peak heat release and point of peak heat release over first acceleration of EUDC phase of drive cycle

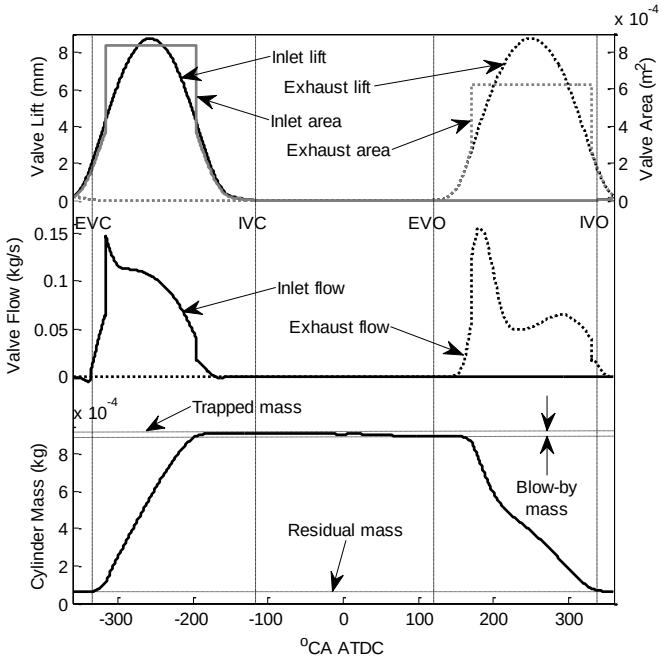

Figure 20 - Valve lift, area and mass flow at 2500rev/min, 120Nm

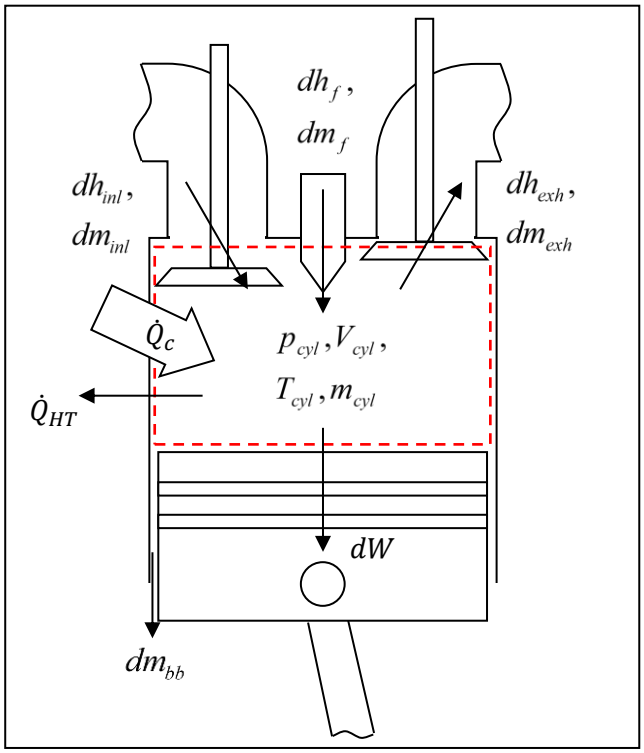

Figure 21 - Single zone model